TEKTONIKA

Unraveling the Kinematics and Morphotectonics of the Petrinja Fault (Croatia), Source of the 2020 M 6.4 Earthquake

Maxime Henriquet [*1,2], **Lucilla Benedetti** [1], **Stéphane Baize** [3], **Branko Kordić** [4], **Marianne Métois** [5], **Josipa Maslač Soldo** [4,6], **Nikola Belić** [4], **Marko Špelić** [4], **Marko Budić** [4], **Daniela Pantosti** [7], **Francesca Cinti** [7], **Stefano Pucci** [7], **Alessio Testa** [8], **Paolo Boncio** [8], **Bruno Pace** [8], **Petra Jamšek Rupnik** [9], **Adrien Moulin** [10], **Riccardo Civico** [7]

[1]Aix Marseille Université, CNRS, IRD, Collège de France, CEREGE, Aix-en-Provence, France | [2]Université Côte d'Azur, CNRS, Observatoire de la Côte d'Azur, IRD, Géoazur, Valbonne, France | [3]Autorité de Sûreté Nucléaire et de Radioprotection, PSE-ENV/SCAN/BERSSIN, Fontenay-aux-Roses, France | [4]Croatian Geological Survey (HGI-CGS), Zagreb, Croatia | [5]Université Claude Bernard Lyon 1, Laboratoire de Géologie de Lyon, France | [6]University of Zagreb, Faculty of Mining, Geology and Petroleum Engineering, Zagreb, Croatia | [7]Istituto Nazionale di Geofisica e Vulcanologia, Roma, Italy | [8]Università G. d'Annunzio Chieti, Pescara, Italy | [9]Geological Survey of Slovenia, Ljubljana, Slovenia | [10]Université Paris Cité, Institut de Physique Du Globe de Paris, CNRS, UMR 7154, Paris, France

Abstract The 2020 Mw 6.4 Petrinja earthquake in central Croatia is one of the European strongest continental earthquakes in recent decades. This event shed light on the poorly investigated Petrinja-Pokupsko Fault (PPKF) zone, a right-lateral fault system accommodating a fraction of the shortening between the Adria and European plates. Through field observations and high-resolution Lidar-derived digital elevation models of the central section of the PPKF, we precisely mapped the fault trace, revealing a discontinuous geometry with a main fault strand and left-stepping segments in agreement with the position of the 2020 surface ruptures. To the north, the accumulated relief from this transpressive fault system decreases, and the fault trace becomes less distinct, suggesting a northward propagation of the deformation. Cumulative offsets of 4 to 24 meters along the main fault strands in the central and southern sections of the fault attest to its Quaternary activity. Dating results suggest offset markers at the Marine Isotopic Stage 4 (MIS 4), the Late Glacial Maximum (LGM) or the Early Holocene periods, allowing for the first direct estimation of the fault slip rates. Preliminary estimates indicate that, assuming a common MIS 4 or LGM age for the investigated markers, fault slip rates range from 0.2 to 0.7 mm/yr and 0.7 to 1.6 mm/yr, respectively. In contrast, assigning Early Holocene ages would imply much higher - and likely unrealistic - slip rates of 1.6 to 3.9 mm/yr. Although the estimated loading rates vary greatly and depend on strong assumptions regarding the age of the markers abandonment, our results suggest a minimum fault slip-rate of 0.2 mm/yr for local seismic hazard assessments.

Executive Editor:
Tony Doré
Associate Editor:
Devin McPhillips
Technical Editor:
Mohamed Gouiza

Reviewers:
Alex Hatem
Reviewer 2
(Anonymous)

Submitted:
3 February 2025
Accepted:
23 February 2026
Published:
9 March 2026

1 Introduction

Within the slow convergence between Africa and Europe, it is now recognized from geodetic strain rates and active tectonics studies that the northward motion and counter-clockwise rotation of the Adria microplate impose shortening across the Dinarides and transpression toward the Pannonian Basin (*Bada et al.*, 2007; *Weber et al.*, 2010; *Métois et al.*, 2015; *Moulin et al.*, 2016; *Serpelloni et al.*, 2016). The resulting north-south contraction in Croatia is outlined by an intense seismicity along the eastern coast of the Adriatic Sea due to the compressional and transpressional deformation in the External Dinarides (*Palenik et al.*, 2019), while the northern part of the country is characterized by a significant intraplate seismicity with rare occurrence of large earthquakes (*Markušić*, 2008). Such kinematics was confirmed in 2020 when central Croatia was hit by two significant earthquakes, the first in March close to the capital Zagreb (Mw 5.4) and second at Petrinja in December (Mw 6.4), 50 km to the southeast (*Markušić et al.*, 2021). This area was however already known as one of the most seismically active regions in Croatia from the analysis of microseismicity and the occurrence of strong historic events (Figure 1) in 1880 (M ~6, Zagreb) and 1909 (M >5.8, Kupa Valley) (*Herak et al.*, 1996; *Markušić*, 2008; *Herak et al.*, 2009; *Herak and Herak*, 2010).

The 2020 Petrinja earthquake is the first documented event with surface ruptures in South Eastern Europe (*Baize et al.*, 2022). This event occurred on the

*✉ ferdinando.musso@unibe.ch

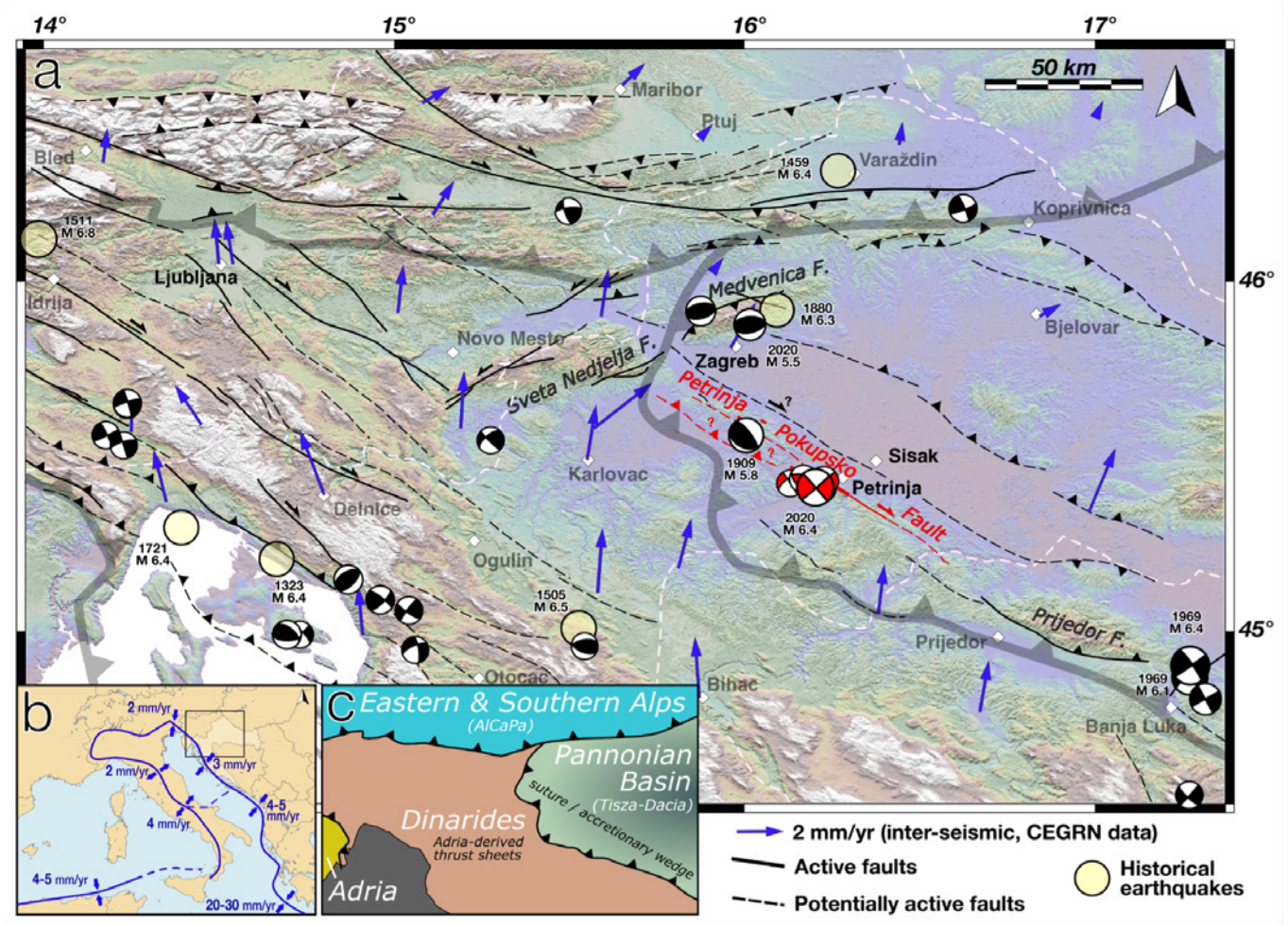

Figure 1 – Seismotectonic map of the SE Slovenia, central Croatia and NW Bosnia and Herzegovina region. The topographic data in the background are from the FABDEM ~30 m resolution worldwide DEM (*Hawker et al.*, 2022). The highlighted active or potentially active faults are compiled from *Tomljenović and Csontos* (2001); *Moulin et al.* (2014, 2016); *Matoš et al.* (2017); *Wacha et al.* (2018); *Atanackov et al.* (2021); *Baize et al.* (2022) and focal mechanisms of instrumental earthquakes with magnitudes M ≥ 4.5 (*Herak*, 2025). Interseismic velocities (blue arrows) are represented relative to stable Eurasia (*Zurutuza et al.*, 2019). Historical earthquakes are from the SHARE European Earthquake Catalogue (SHEEC (*Stucchi et al.*, 2013; *Grünthal et al.*, 2013). The Petrinja-Pokupsko Fault (PPKF) is highlighted in red and the Petrinja section that ruptured in 2020 is in full line. Note the uncertainties on the fault continuity and structure toward the NW in the epicentral area of the 1909 Pokupsko earthquake. Dotted white lines represent country borders. Inset: present-day regional kinematics of the Adriatic region (*Nocquet*, 2012) and main structural units in the wider area.

Petrinja fault, the central portion of the SE-striking Petrinja-Pokupsko fault system (PPKF) that belongs to a >100 km long fault system extending from the southern flank of the Kozara mountains in Bosnia (Prijedor fault) to the NE-striking Sveta Nedelja – Medvenica faults, west and north of Zagreb (Figure 1). A post-seismic survey revealed a segmented SE-striking surface rupture over ~13 km, with a mean dextral slip of ~10 cm (*Baize et al.*, 2022). Geodetic slip inversions (*Ganas et al.*, 2021; *Xiong et al.*, 2022; *Henriquet et al.*, 2022; *Zhu et al.*, 2023) constrained a shallow (3–13 km), dextral and steeply dipping source (>70°) toward the SW, in agreement with the focal mechanisms and relocated aftershocks (*Baize et al.*, 2022; *Herak and Herak*, 2023). The PPKF is included in a NE-dipping composite source with reverse kinematics in the European Database of Seismogenic Faults (EDSF) from *Basili et al.* (2013, 2024), with the northern part of the PPKF hypothesized as the source of the 1909 Kupa Valley earthquake (*Herak and Herak*, 2010). The PPKF reported in EDSF is incompatible with the geometry and kinematics of the 2020 rupture that occurred on a steep, NW-trending, SW-dipping plane with a dextral strike- slip kinematics; this suggests that different seismic source characterize the central part of PKKF and that the definition of the PPKF in the EDSF needs to be updated.

The 2020 sequence highlights the poor knowledge of the intracontinental faults in this region and shows that substantial work is required to better understand the fault behavior. Several questions arise concerning the PPKF and some of them directly impact the seismic hazard that could be assigned to the PPKF and/or to the composite source. For instance, *Basili et al.* (2013, 2024) assume that the composite source related to the PPKF can produce a maximum magnitude of 6.5 events. However, the 6.4 magnitude of the 2020 earthquake questions the reliability of this Mmax, as it did rupture only a part of the entire PPKF ESDF structure opening

the possibility that multisegment ruptures may occur. In the same line, the slip rate between 0.08 and 0.2 mm/yr proposed by *Basili et al.* (2013, 2024) is not supported by observed geological data and could represent a lower bound, considering the preliminary observations of large offsets (>250 m) of geomorphic features preserved in the landscape (*Baize et al.*, 2022; *Henriquet et al.*, 2021; *Jamšek Rupnik et al.*, 2021). Mapping of active faults and estimating their slip-rates is particularly challenging in slowly deforming regions where expected slip-rates barely reach a few mm/yr, but also when vegetation and human activities are widespread such as in Europe. Nevertheless, recent studies have shown that high-resolution (~1m) Lidar-derived Digital Elevation Model (DEM) can provide robust constraints on offset geomorphic markers along strike-slip faults in similar settings such as the Idrija and Sava faults in Slovenia (*Moulin et al.*, 2014, 2016; *Jamšek Rupnik et al.*, 2024). In this paper, we take advantage of a 25-km-long Lidar DEM acquired after the 2020 Petrinja earthquake to map the Petrinja Fault, and identify, quantify, and date cumulative geomorphic offsets to estimate the long-term (Quaternary) fault slip-rate.

2 Regional Tectonic Setting

Central Croatia lies within the junction between the Alps, the Dinarides and the Pannonian Basin (Figure 1c), a region that experienced multiple phases of deformation in response to the Alpine-Dinaric orogeny (*Schmid et al.*, 2008, 2020; *Horváth et al.*, 2015). The subduction of the Neotethys under the European margin ended during the Late Cretaceous to early Paleogene, and it is marked by the Sava suture zone (e.g., *Pamić*, 2002; *Schmid et al.*, 2008, 2020; *Ustaszewski et al.*, 2010). Early Cretaceous to Paleogene syn-orogenic deposits attest to the coeval imbrication of tectonic units (*Pamić*, 2002; *Tomljenović et al.*, 2008; *Vukovski et al.*, 2024). This phase was followed by the migration of compressive deformation from the Sava suture zone to the External Dinarides, forming a foreland during the Mid-Eocene (*Schmid et al.*, 2008; *Brčić et al.*, 2023). The mentioned convergence between Adria and Europe culminated in in-sequence thin and thick-skinned thrusting which resulted in accreting Adriatic Carbonate Platform shallow-marine formations units (*Vlahović et al.*, 2005) and older Mesozoic and Paleozoic basement (e.g., *Tari*, 2002; *Korbar*, 2009; *van Unen et al.*, 2019; *Balling et al.*, 2021; *Špelić et al.*, 2023).

The continuous continental collision between Adria microplate and Europe led to the lateral extrusion of the Eastern Alps (*Horváth et al.*, 2006; *Rosenberg et al.*, 2018), and NE-SW diachronous back-arc extension within the AlCaPa and Tisza-Dacia units due to the subduction retreat of the European slab beneath the Carpathians (e.g., *Royden and Horváth*, 1988; *Ustaszewski et al.*, 2008; *van Hinsbergen et al.*, 2020). In modern coordinates, this extension phase was accommodated by NNW-SSW striking normal and strike-slip faults during Miocene times from ~20 Ma to ~8 Ma, and locally the reactivation of former structures from the Eastern Dinarides produced low-angle detachments such as the NW-SE trending Sava and Drava basins (e.g., *Tomljenović and Csontos*, 2001; *Horváth et al.*, 2006; *Ustaszewski et al.*, 2010; *Balázs et al.*, 2016; *Rukavina et al.*, 2023). This extensional episode was followed by a Late Miocene post-rift thermal subsidence phase (*Royden and Horváth*, 1988) with coeval high sedimentation rates that filled these basins (*Magyar et al.*, 2013).

During the Pliocene and the Quaternary, the continuous N-NE directed indentation of Adria built up compressional stresses in the Pannonian basin (*Bada et al.*, 2007). Such late stage of compression led to the basin-wide tectonic inversion of previous extensional and strike-slip faults (*Horváth et al.*, 2006; *Bada et al.*, 2007; *Horváth et al.*, 2015), visible both with surface and reflection seismic data showing tilted and deformed Late Miocene deposits (7.1–5.6 Ma) (Figure 2b). The deformation concentrated on marginal Sava and Drava basin detachments and connected normal systems, as well as the Periadriatic Fault and its eastward prolongation into the Mid-Hungarian fault zone that separates the AlCaPa and Tisza-Dacia blocks (e.g., *Royden and Horváth*, 1988; *Tari and Pamić*, 1998; *Tomljenović and Csontos*, 2001; *Ustaszewski et al.*, 2014; *Wacha et al.*, 2018). The formation of these large-scale fault-related folds, 'pop-up' and positive flower-structures in central and northern Croatia also resulted with tectonic uplift that likely shaped the main reliefs along these fault systems (*Prelogović et al.*, 1998; *Tomljenović and Csontos*, 2001; *Matoš et al.*, 2017; *Pavičić et al.*, 2019, and references within), such as the Medvednica hills north of Zagreb and the Hrastovica hills, along the Petrinja section of the PPKF (Figure 2). Currently, although the lack of GPS data in Croatia and Bosnia precludes any accurate strain rate estimation (*Métois et al.*, 2015), the <5 mm/yr of NNE-SSW shortening between Adria and Europe seems distributed over >150 km within the External Dinarides and the western Pannonian basin. Such activity in Central Croatia is evidenced by the current seismicity, mainly localized along the SE-striking PPKF and the NE-striking Medvednica Fault systems (*Herak et al.*, 2009, Figure 1).

Along the studied central portion of the PPKF, the Miocene and Plio-Quaternary deposits overlay Jurassic to Eocene units that locally crop out in the Hrastovica hills (Figure 2 *Pikija*, 1987; *Šikić*, 2014). The Upper Miocene and Plio-Quaternary units are mostly composed of fluvio-lacustrine deposits made of conglomerates, sandstones, marls, sands, gravels, and clays, while older outcropping Middle Miocene deposits (Badenian) are represented by calcarenites and limestones (*Pikija*, 1987; *Pavelić and Kovačić*, 2018). Finally, the Pleistocene aeolian loess and fluvial to colluvial deposits cover most of the low relief zones surrounding the Hrastovica hills.

Baize et al. (2022) showed that the PPKF is a deep-seated dextral strike-slip fault zone with a clear positive flower structure (Figure 2b), with Badeninan or locally Paleogene and Cretaceous basement units

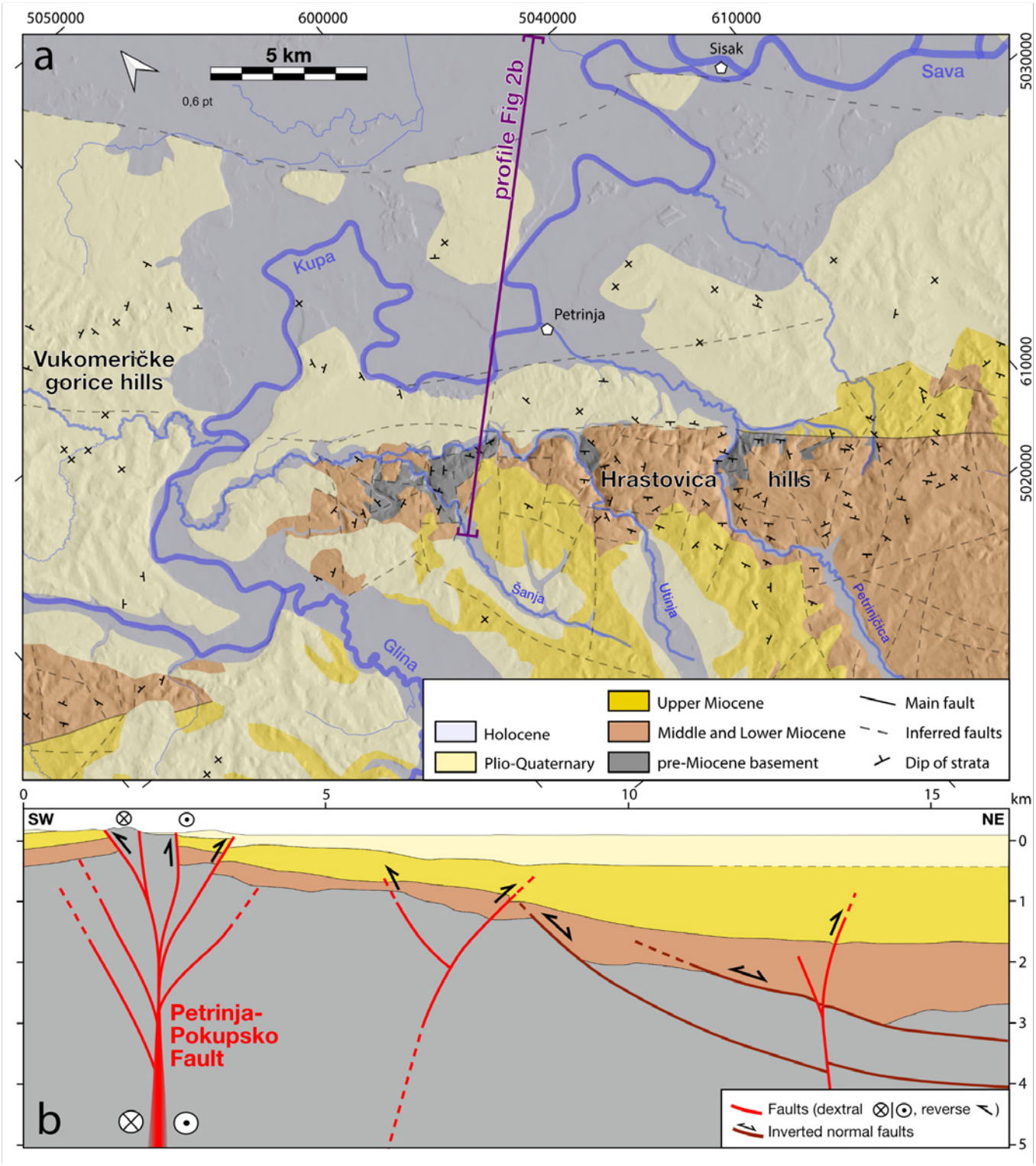

Figure 2 – Geological map **(a)** and cross section **(b)** of the Petrinja area. The geological map is simplified from *Pikija* (1987) and *Šikić* (2014). Main and inferred faults are reported together with dipping of strata. The geological cross section shows the regional structural and stratigraphic relations, modified from *Baize et al.* (2022) based on a seismic section across the Sava plain. The Hrastovica hills forms the core of the inferred positive flower structure, which accommodates oblique shearing and vertical deformation resulting from local compression on the Petrinja Fault.

reversely displaced on Plio-Quaternary deposit. The Hrastovica hills. represents SE trending anticline with mentioned pre-Neogene basement units cropping out along the PPKF central part, overlain by Neogene deposits, tilted in the form of SE trending anticline. The southwestern limb gently dips towards the Glina sub-basin without major deformations, whereas the northeastern limb dipping towards the Sava Basin is cut by the PPKF. In contrast, the NE limb is characterized by the positively reactivated NE-dipping listric faults (low angle faults in the Figure 2b), which controlled the syn-rift Sava Basin formation (*Baize et al.*, 2022). According to *Baize et al.* (2022), the interpreted unconformity in the Upper Miocene suggests that the

PPKF and the related Hrastovica hills uplift may have been initiated at that time, during the start of the Pannonian Basin tectonic inversion (*Bada et al.*, 2007).

3 Morphotectonic Trace of the Petrinja Fault from High-resolution DEMs

Our detailed geomorphic analysis of the PPKF mostly relies on an airborne Lidar dataset that was acquired in 2021, two months after the 2020 Petrinja earthquake (*Baize et al.*, 2022). The dataset covers a length of 29 km and a width of 3-5 km along the section that ruptured in 2020, from the Kupa River to the northwest to Gornja Budičina to the southeast (Figures 3 and 4). A small portion (2 × 1 km) of the dataset was processed and published in *Baize et al.* (2022). We process here and analyze the entire swath to obtain high-density point cloud data (~6 pts/m^2 in forest area, ~8 pts/m^2 in non-vegetated areas) on the ground surface after vegetation points were removed, and generated a DEM at a resolution of 0.5 m and locally 0.2 m. The geomorphic analysis also benefited from field observations, the ALOS World 3D 30 m DEM (AW3D30), WorldView-derived tri-stereo DSMs (~1 m resolution), orthophoto images from State Geodetic Administration and UAS datasets, geological data (*Pikija*, 1987; *Šikić*, 2014) and the seismic-reflection from the Croatian Hydrocarbon Agency interpreted in *Baize et al.* (2022).

3.1 Fault and Fold Mapping

The high-resolution topographic dataset compiled in this study allows the recognition of recent fault motion from various geomorphic markers (drainage network, alluvial terraces, and fans). Along the studied Petrinja Fault, there is a clear 10-km-long segment striking ~N132° between Gornja Budičina and the Utinja river, called Southern Petrinja Fault (SPF, Figure 3b), stepping to the left toward the northwest. The surface ruptures from the 2020 earthquake were mostly localized along the central (Cepeliš-SPF, CSPF, Figure 3b) and northern sections (Župić Relay Zone, ZRZ, and Northern Petrinja Fault, NPF, Figure 3b) of the Petrinja Fault, consistently with the main long-term fault traces, i.e. the trace left in the landscape during the Quaternary. Actually, the main fault segment is the SPF, composed of 2-3 sub-parallel fault sections that accommodate the deformation within a 200-600 m wide fault zone. This main segment possibly continues to the SE for up to 4 km outside the Lidar covered area, but this interpretation is hampered by the low quality of the Pléiades-derived DSM in this highly vegetated zone and the high density of landslides.

The southeastern part of the SPF delimited to the NW by the Petrinjčica river (Donja Budičina-SPF, DBSPF, Figure 3b) cuts the foothill over 2 km. From the southeast, the DBSPF is composed of 3 strands, striking from N130° (basin ward) to N143° (relief ward), and connecting on the main central segment that follows the main slope break of the Hrastovica hills ~500 m NW of Gornja Budičina. Toward the northwest along the DBSPF, the main central strand still follows the Hrastovica hills front, while inferred subparallel secondary strands localize ~100 m away along the main relief front (dashed red line under Donja Budičina, Figure 3b) and ~700 m from the main segment within the Hrastovica hills (dashed red line above the "D" of "DBF", Figure 3b).

Toward the northwest, the main strand keeps following the NE-border of the Hrastovica hills between Petrinjčica and Utinja rivers (Cepeliš Southern Petrinja Fault, CSPF, Figure 3b). However, large deep-seated landslides characterized by circular scars SW from the Hrastovica village perturb the straight and steep (~40°) foothill of the Hrastovica hills and locally disturb the observation of continuous fault segments on the southeastern portion of the CSPF. The main segment identified in this area runs from Hrastovica to the Petrinjčica river SE-ward over 1.5 km, striking N143°. North-westward on the CSPF, the Cepeliš segment shows 4 SE-diverging strands striking from N163° (relief ward) to N125° (basin ward). Among those segments, two main strands called Cepeliš Main Upper Strand (CMUS) and Cepeliš Main Lower Strand (CMLS, Figure 5c), about 3 km-long and 200-300 m apart, cut the middle and the base of the Hrastovica hills, striking N143° and N133° respectively. The secondary segments respectively called Cepeliš Secondary Upper Strand (CSUS) and Cepeliš Secondary Lower Strand (CSLS, Figure 5c), first connect to the main strands south of Cepeliš, and the CMUS up-hill seems to connect to the CMLS down-hill before reaching the Utinja valley, where a large landslide disturbs the continuity of the CSPF along the Hrastovica flank (Figure 3b). The main lower strand seems to continue within the Utinja valley up to Križ, while another segment striking N140° cuts a large alluvial fan at the foot of the Hrastovica hills on the left-side of the river and vanishes SE-ward within the relief. We also note that linear escarpments striking ENE are visible on the Figure 5 and could be confused with active fault traces. However, no Quaternary markers appear to be offset along these lineaments, so we assume they result from surface erosive processes potentially localized on ancient faults or lithological contacts.

The fault system continues to the northwest from Križ (Župić Relay Zone, ZRZ, and Northern Petrinja Fault, NPF, Figure 3b), but the fault segments are much less preserved and likely shorter (~500 m). Further north near Župić and northward, two segments are inferred. One appears very discontinuous along the Utinja River stretching from Župić to Gornje Mokrice to the northwest. The second cuts the quarry south of Župić and seems to connect with the inferred E-W south-verging thrust bordering the uplift axis west of Župić in the Župić Relay Zone (ZRZ, Figure 3b). These compressional features are compatible with the change in strike (~N10°) and the right-lateral kinematics of the fault system making a restraining bend. The last recognized segments northwest of the Šanja river cross the lower relief of the eastern flank of the Hrastovica hills (NPF, Figure 3b). Two parallel strands striking around N142° are separated by about 250 m between Međurače

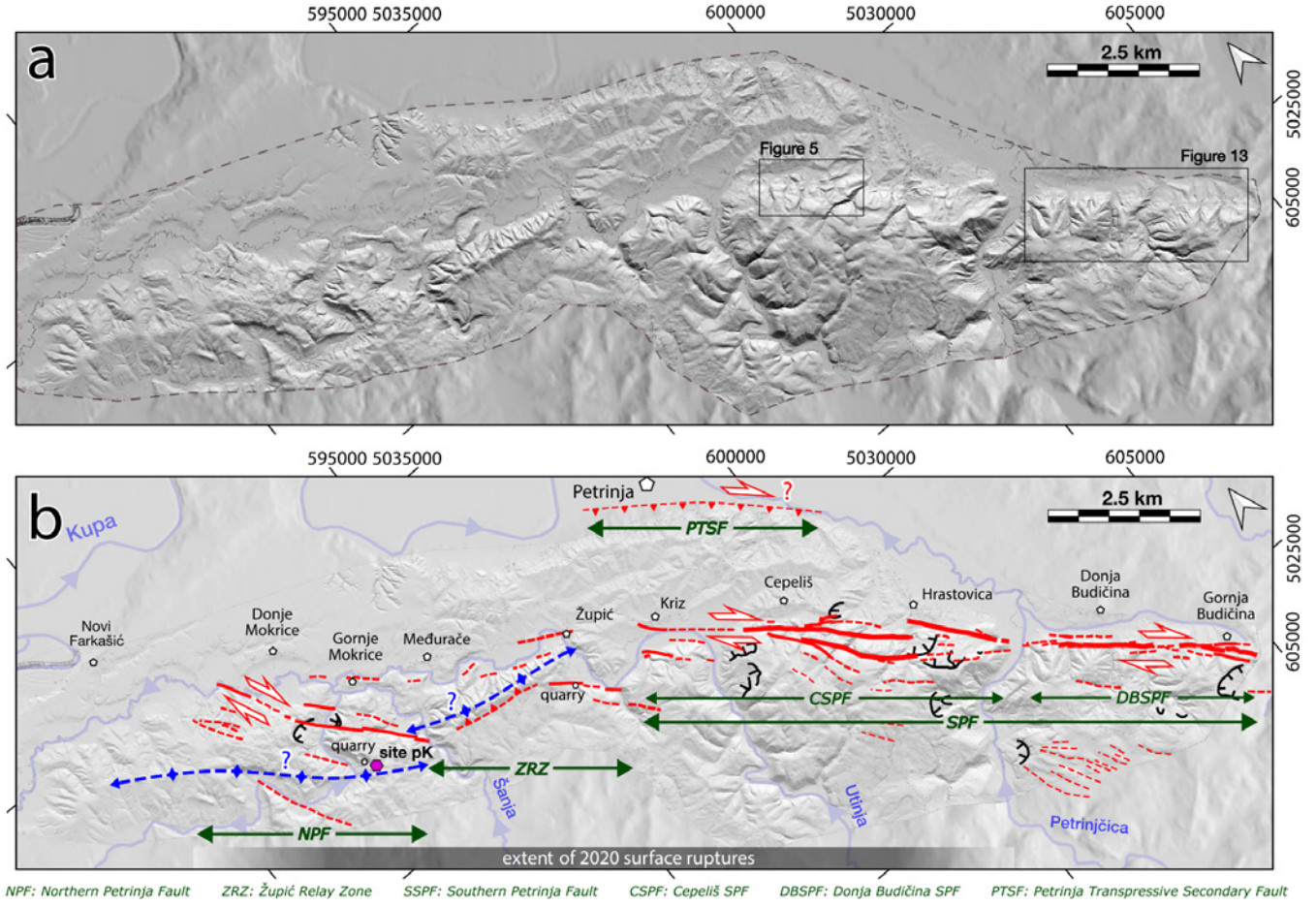

Figure 3 – Fault trace map along the ruptured Petrinja Fault, the central section of the PPKF. The shaded relief map is produced from the LiDAR dataset acquired after the 2020 Petrinja earthquake (resolution 50 cm). The dashed polygon in the panel a shows the extent of the area covered by LiDAR data). Dashed red lines represent inferred active fault traces and potential active folds or uplift axis are drawn in blue. Main landslides are in black. The Petrinja Fault can be divided in 3 parts from the southeast to the northwest: the Southern Petrinja Fault (SPF), including the Donja Budičina section (DBSPF) and the Cepelis section (CSPF), then the Župić Relay Zone (ZRZ) constitutes the transition toward the Northern Petrinja Fault (NPF). The SPF is characterized by straight fault strands while the deformation appears more distributed northwards. The 2020 surface ruptures were localized on the CSPF, ZRZ and NPF sections. The site pK corresponds to the site where alluvial conglomerates and sands were found along the edge of the incision of the "paleo-Kupa".

and the quarry to the west, and small sections with a similar orientation are inferred within the Hrastovica hills and along the Utinja river.

At a broader scale, the surface trace of the PPKF shows a clear difference between the NPF, north of Križ, where the preserved deformation is characterized by short left-stepping segments, and the SPF mostly made of 2-3 sub-parallel strands delimiting the sharp eastern flank of the Hrastovica hills. The left-stepping segmentation of the NPF locally produces a restraining bend configuration that seems to explain the generation of reliefs, extending the Hrastovica hills up to the Kupa valley.

Based on the DEM analysis and the geological map (Pikija, 1987), the Petrinja Fault section might continue to the north of the Kupa river in the epicentral area of the 1909 Kupa Valley earthquake. A straight system of NW-SE oriented valleys starting from the Kupa river and extending for ~35 km along the drainage divide of the Vukomeričke gorice hills suggests that the Pokupsko section of the PPKF continues on a significant strike-slip strand to the NW (Figure 4a). However, the SW-verging fault inferred by Herak and Herak, (2010) as the source of 1909 Kupa Valley earthquake is not highlighted by a clear asymmetry of the Vukomeričke gorice hills, that rather shows a badland morphology possibly due to a slight uplift of Plio-Quaternary sediments on both side of the Pokupsko strike-slip segment. Toward the southeast, fault trace continues for several kilometers and then becomes less clear when crossing the Sunja valley and the Bosnia border, but likely reaches the Prijedor fault system north west of Banja Luka in Bosnia (Figure 1).

3.2 Geomorphological Markers of Uplift

The NW-SE oriented Hrastovica hills extends about 35 km from the Kupa river to the north to the Sunja valley to the south, and its mean width is around 4 km (Figure 4). The northern part of the hills lies at a lower elevation (~200 m a.s.l.) than the southern part (300-400 m a.s.l.), with an abrupt transition near Križ and a culmination between the Petrinjčica and Utinja rivers (415 m). The local base level corresponds to the Sava plain at ~100 m

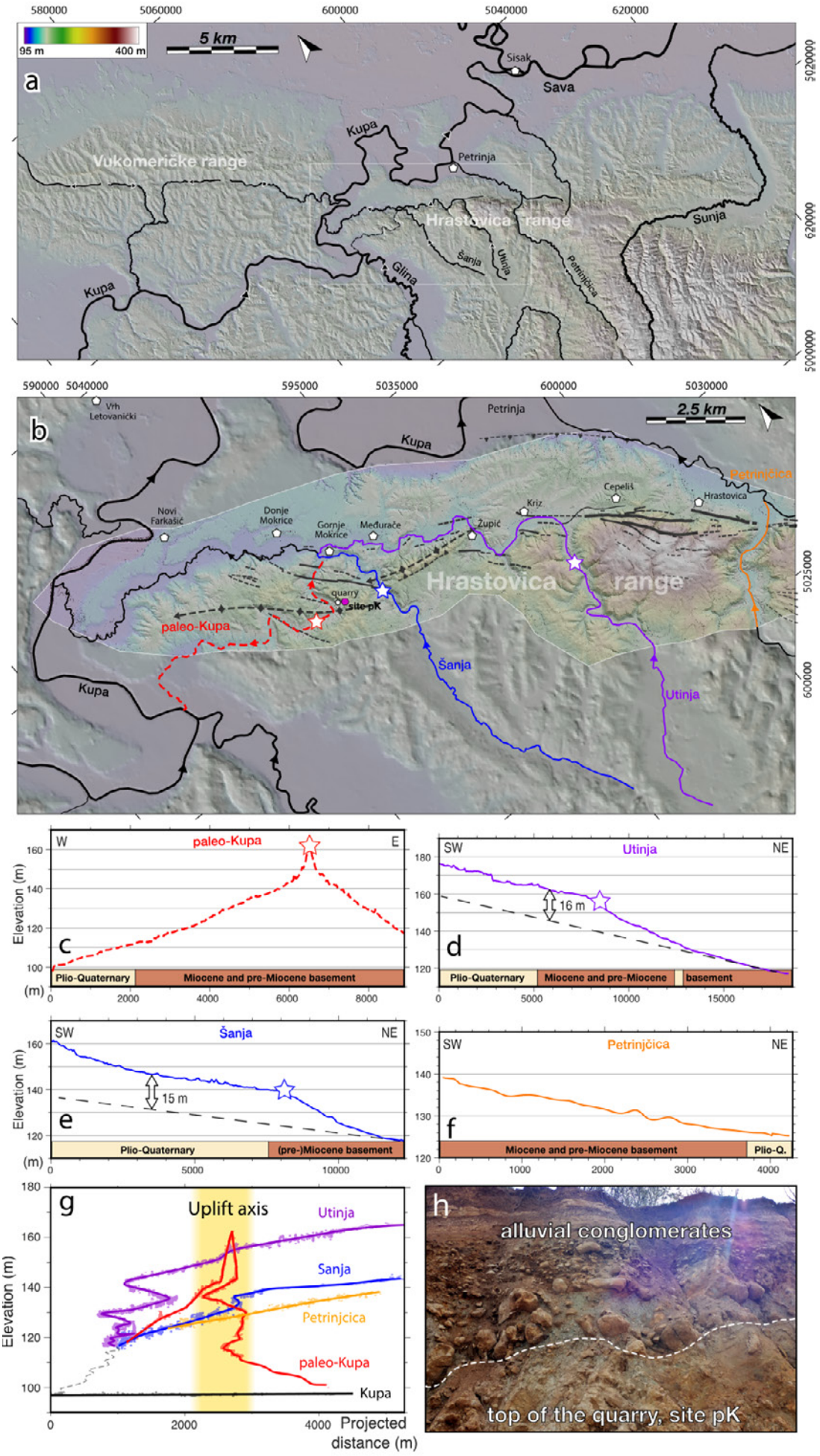
a
5 km
95 m
400 m
Sisak
Sava
Kupa
Petrinja
Vukomeričke range
Hrastovica range
Sunja
Šanja
Utinja
Petrinjčica
Glina
b
2.5 km
Vrh Letovanički
Novi Farkašić
Donje Mokrice
Gornje Mokrice
Međurače
Župić
Križ
Cepelić
Hrastovica
quarry
site pK
paleo-Kupa
c
paleo-Kupa
W
E
Elevation (m)
Plio-Quaternary
Miocene and pre-Miocene basement
d
Utinja
SW
NE
16 m
basement
e
Šanja
15 m
(pre-)Miocene basement
f
Petrinjčica
Plio-Q.
g
Uplift axis
Sanja
Petrinjcica
Projected distance (m)
h
alluvial conglomerates
top of the quarry, site pK

Figure 4 – Hydrographic maps of the Petrinja area and longitudinal profiles of the main rivers across the PPKF. Large scale topographic data are from the FABDEM ~30 m resolution worldwide DEM (*Hawker et al.*, 2022) and locally from the ~50 cm resolution LiDAR dataset acquired along the 2020 rupture (white polygon on panel b). The map view in panel a and b shows the NW diversion of the rivers and the location of drainage along the fault on the NE flank of the Hrastovica hills. The long-term fault trace from Figure 3 is represented in the background. The river profiles from panels c to f highlight potential river disequilibrium, such as the knickpoints on the Utinja and Šanja rivers upstream from the PPKF, or the major wind gap of the paleo-Kupa river. At the bottom of each profile the main lithological units in which the rivers are incising are represented. The panel g shows the same rivers projected across strike with an azimuth of ~50°. The photo in panel h shows the alluvial conglomerates left on the edge of the paleo-Kupa canyon, on top of the quarry (site pK where samples Q_1, Q_3 and Q_3 are taken for cosmogenic dating).

a.s.l. In its southern high-relief section, the northeastern (Petrinja) side of Hrastovica hills is characterized by a stronger topographic gradient along the fault system, in agreement with the highest relief mapped by *Bočić* (2021). Between the Hrastovica hills and Petrinja a second topographic step sub-parallel to the Hrastovica hills and ~100 m above the Kupa extends from the Hrastovica village >10 km to the northwest.

A strong lithological contrast follows the main fault strand (*Pikija*, 1987; *Šikić*, 2014; *Jamšek Rupnik et al.*, 2021; *Baize et al.*, 2022, Figure 2), with stiff sedimentary units (Miocene and pre-Miocene, esp. Badenian calcarenites and detrital and clastic deposits) making the reliefs southwest of the fault, and loose units to the NE (Plio-Quaternary, e.g. lacustrine and fluvial clays and sands, loess). In general, the Hrastovica hills is characterized by a dominantly covered karstic relief with deeply incised valleys, numerous dolines and sinkholes visible in the topographic maps, and frequent stream sinks and abandoned valleys. Most of the springs draining the karst are located along the fault-system. Along the fault from Gornja Budičina to Cepeliš, drainage is denser on the basin side, incising the Plio-Quaternary with wider valleys (U-shape), than on the Hrastovica hilly side (strongly incised V-shaped valleys). This difference can result both from strike-slip tectonics (beheaded streams) and/or recent regressive erosion blocked against the strong lithological contrast.

At large scale, the wide valleys of Petrinjčica, Utinja and Šanja rivers are characterized by deeply incised valleys when crossing the Hrastovica hills, and together with the larger Kupa River, they show at first order a NW-oriented diversion (Figure 4a and 4b). This observation suggests the progressive north-westward propagation of uplift, which forces the rivers to divert north-westward around the emerging relief of the Hrastovica hills, the core of the positive flower structure (Figure 2b). Locally, it has also been reported a higher stream sinuosity at the intersection with the fault trace, which has been attributed to a possible dip-slip component of the fault kinematics by *Jamšek Rupnik et al.* (2021). Significant large-scale knickpoint (~15 m high spread over 1 to 5 km) within the Utinja and Šanja rivers aligned with the relief axis and might outline the uplift of the Hrastovica hills (Figure 4d and 4e). Although precautions must be taken, as a significant lithological contrast on either side of the fault and on the SW side of the Hrastovica hills, we note that the large-scale knickpoints does not match with lithological contrasts between the Plio-Quaternary deposits and the Miocene and pre-Miocene basement, which discard the differential erosion along the rivers as the main controlling factor of river disequilibrium. Another evidence of uplift lies in the northwest of the Hrastovica hills, between the Utinja and Kupa rivers, where a major windgap (inactive water course) fully crosses the karstic plateau from west to east (*Bočić*, 2021; *Henriquet et al.*, 2021). Morphologically, it looks like a ~400-600 m wide and 50-80 m deep meandering paleo-valley, similar to the perched Čepovan Canyon in Slovenia (*Moulin et al.*, 2016). Today, diverging streams flow westward and eastward from the windgap bottom pass (Figure 4c). Young alluvial conglomerates and sands (Figure 4h) were found along the edge of the incision (on top of the operated quarry, site pK in the Figure 3b and 4b) and might mark the former course of the drainage before its incision. It is indeed interpreted as the former course of the Kupa river that has been abandoned with the uplift of the Hrastovica hills. Unfortunately, no alluvial deposit remains at the pass within the windgap that could be sampled and dated to estimate an uplift rate, possibly because strong stream incision continued after the valley was abandoned by the Kupa river as testified by the two concave upstream shapes on both sides of the windgap (Figure 4c).

4 Cumulative Lateral Displacements along the PPKF

To estimate the long-term displacements along the Petrinja Fault (central part of the PPKF), we used offsets of morphological markers by extrapolating piercing lines up to the mapped fault trace. As piercing lines, we used thalwegs, streams, hill crests and terrace risers. We then test the estimated offsets by back-slipping along the fault and propose a range of plausible cumulative displacements. The limited extension of the fault covered by Lidar data, the vegetation cover in this temperate climate and the slow deformation rate with respect to active erosion rate prevent the identification of numerous offset markers along the studied section. Moreover, surface ruptures from the 2020 Mw 6.4 earthquake show maximum localized slip <30-40 cm (*Baize et al.*, 2022), a displacement magnitude likely too small to be preserved as a single feature whereas larger relative displacements (>1 m, *Henriquet et al.*, 2022) across ~100-500 m wide bands could be measured from geodetic analyses. Because of this, we focused on long-term cumulative

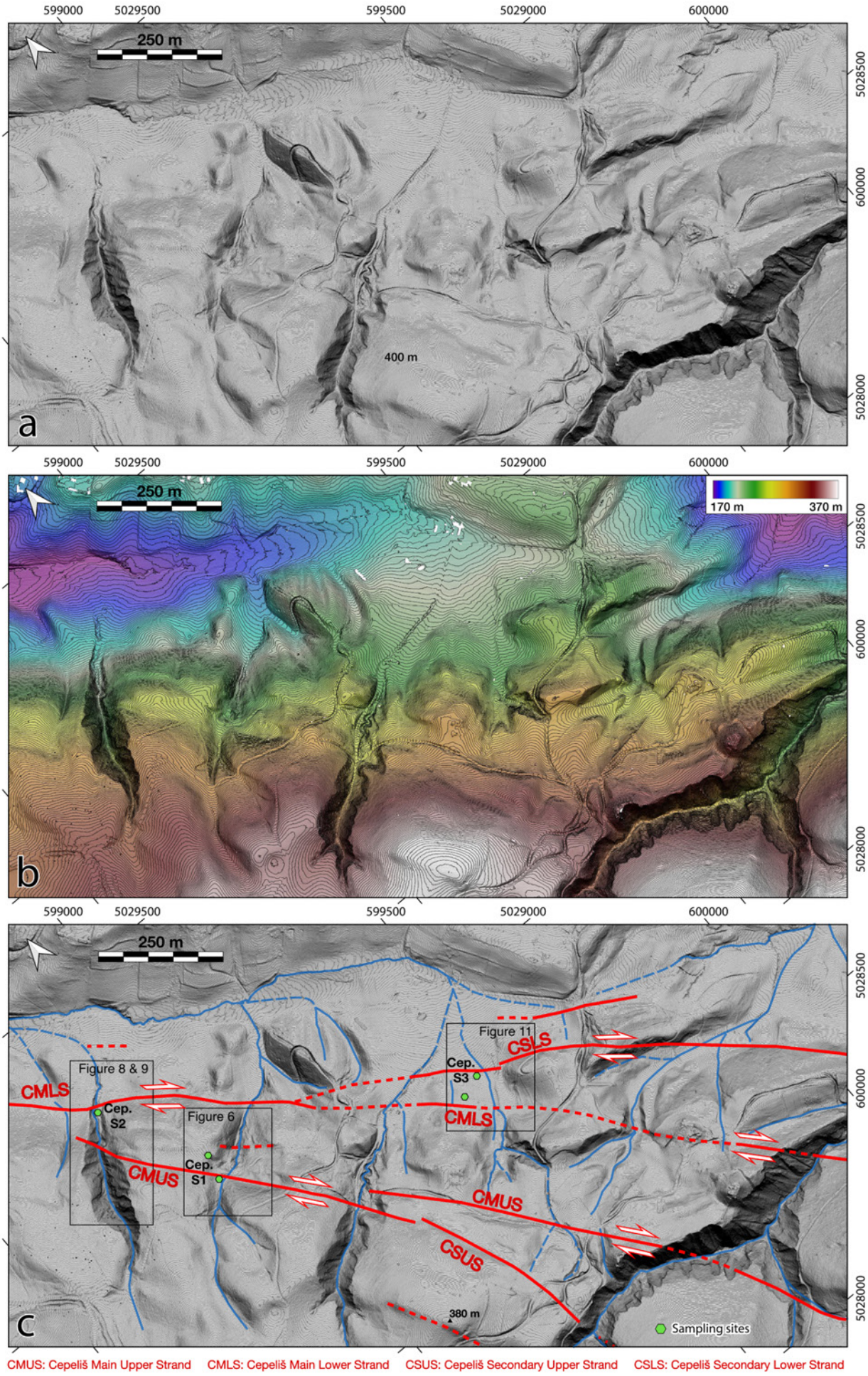
599000
5029500
599500
5029000
600000
250 m
5028500
600000
5028000
400 m
a
b
170 m
370 m
c
Figure 8 & 9
Figure 6
Figure 11
CMLS
CSLS
CMUS
CSUS
Cep. S1
Cep. S2
Cep. S3
380 m
Sampling sites
CMUS: Cepelišć Main Upper Strand
CMLS: Cepelišć Main Lower Strand
CSUS: Cepelišć Secondary Upper Strand
CSLS: Cepelišć Secondary Lower Strand

Figure 5 – Morphotectonic map showing the fault trace along the Cepeliš section of the PPKF. The spacing between the contour lines draped on the shaded relief maps is 50 cm on panels a and c and 1m on panel b. The black rectangles show the location of the investigated sites where displaced geomorphic markers are quantified. The purple hexagons represent sample locations for cosmogenic or charcoal dating. Note that the fault splits on two main branches, the Cepeliš Main Upper Strand (CMUS) and Cepeliš Main Lower Strand (CMLS), with secondary strands connecting to the main branches, the Cepeliš Secondary Upper Strand (CSUS) and Cepeliš Secondary Lower Strand (CSLS), up-hill and down-hill respectively.

offsets and slip rates instead of attempting to reconstruct an earthquake recurrence model.

The main uncertainties for offset measurements mainly come from the orientation of the marker relative to the fault, its sinuosity and continuity across the strike, the fault width and the differential erosion due to lithological variations across the fault (*Ferrater et al.*, 2015). To estimate cumulative displacements of geomorphic markers that could also be reliable for Quaternary dating, we studied in detail four sites along the mapped fault trace. Three sites are located along the Cepeliš Southern Petrinja Fault (CSPF), and one site near Gornja Budičina at the southeastern extremity of Donja Budičina Southern Petrinja Fault (DBSPF, Figure 3).

4.1 Cepeliš Sites

The Cepeliš section constitutes the central part of the CSPF, with a clear expression of the long-term fault trace (Figures 3 and 5). The fault splits into 4 strands that converge toward the Utinja river to the NW (CSUS, CMUS, CMLS and CMUS from up-hill to down-hill, Figure 5c and section 3.1). These fault strands follow the northeastern slopes of the Hrastovica hills; upstream, they intersect deep valleys incised by seasonal streams (>50 m deep, spaced about 300m apart), whereas downstream they cross alluvial fan and slope wash deposits.

At the foot of the main relief, a river sub-parallel to the fault drains these streams towards the Utinja river and likely flows along the limit between two main lithological units (Figure 5). Upslope and on the Hrastovica hills the sharp reliefs are mostly supported by the Badenian calcarenites, whereas on the NE-side of the fault the weaker Plio-Quaternary units lead to smoother and lower reliefs. This first-order geological contact underlines the large-scale fault trace and the fault pattern is associated with a staircase topography, i.e. the hillside is divided into steep flanks and flat surfaces. that suggests a dip-slip component on most strands. We focused our analysis of offset geomorphological markers on the main strand of the upper branch CMUS (Cepeliš S1 and S2a, Figures 6, 7, 8 and 10) and on the lower branches CMLS and CSLS (Cepeliš site S2b, S3, Figures 9, 11 and 12). The corresponding offsets are described in detail hereafter.

4.1.1 Cepeliš S1 – SE-site on the CMUS

The Cepeliš S1 site is located on the CMUS striking ~N140° (Figures 5 and 6). Due to colluvium cover and thick soil and vegetation development, the fault plane is not visible with the exception of one outcropping fault plane ~100 m SE of the intersection between the morphological trace of the fault and the stream (Figures 6a and 7c). This smooth plane, approximately 1.5 m high and 0.5 m wide, has a strike azimuth of ~160° and dips at 80° to the ENE. It exposes the Badenian limestones but the lack of slickensides prevents a clear analysis of the fault kinematics there. About 60 m downstream, a second fault strand outlined by a steep and counter-slope escarpments possibly crosses the incised valley (Figure 6).

Along the main fault strand, a slope break and low-dipping surfaces (<15°) interrupts the steep flank of the Hrastovica hills. We cleaned an outcrop bounding the track that goes up to the surface north of the drain (Cep S1 profile, Figure 6a) and we found that the first two meters are composed of colluvial centimetric clasts (Figure 7b).

At this site the incision of the stream is shallower (<40 m) with respect to the surrounding ones to the NW and to the SE (Figure 5c), in particular between the main and the secondary fault segment (<25 m). The stream flows perpendicular to the main fault segment and is deflected toward the right when crossing the fault zone (Figure 6a). Interestingly, the right bank upstream of the main fault is steeper than the left bank slope (~45° against ~40°) (by convention right and left banks are defined while looking downstream), whereas it is the opposite downstream of the potential secondary fault (43° against 47°). Such stronger erosion of the inner banks relative to the deflection center might suggest that the lateral erosion is ongoing and contemporaneous with the right-lateral slip along the fault.

The clastic material transported by the seasonal stream is Badenian limestone, from gravels to boulders up to several tens of centimeters in size. The catchment area of the stream is quite small, <0.05 km^2 from the main fault trace. The slope of the stream bed is high, about ~10° on average, and between the main and the secondary fault strand up to >20°. The elevation difference between the upstream and downstream projected river bed outlines a >50 m wide and 12-17 m high knickpoint (Figure 6c). While at a larger scale this knickpoint might coincide with the fault trace, we show here that the main slope break occurs downstream the studied fault segment. Therefore, we cannot infer that such vertical motion on this site corresponds to the dip-slip kinematics component on the upper branch of the fault only. This observation suggests that the origin of the knickpoint is downstream, perhaps due to the lithological contrast in this zone that is difficult to locate precisely, or to the activity of the lower branch of the fault.

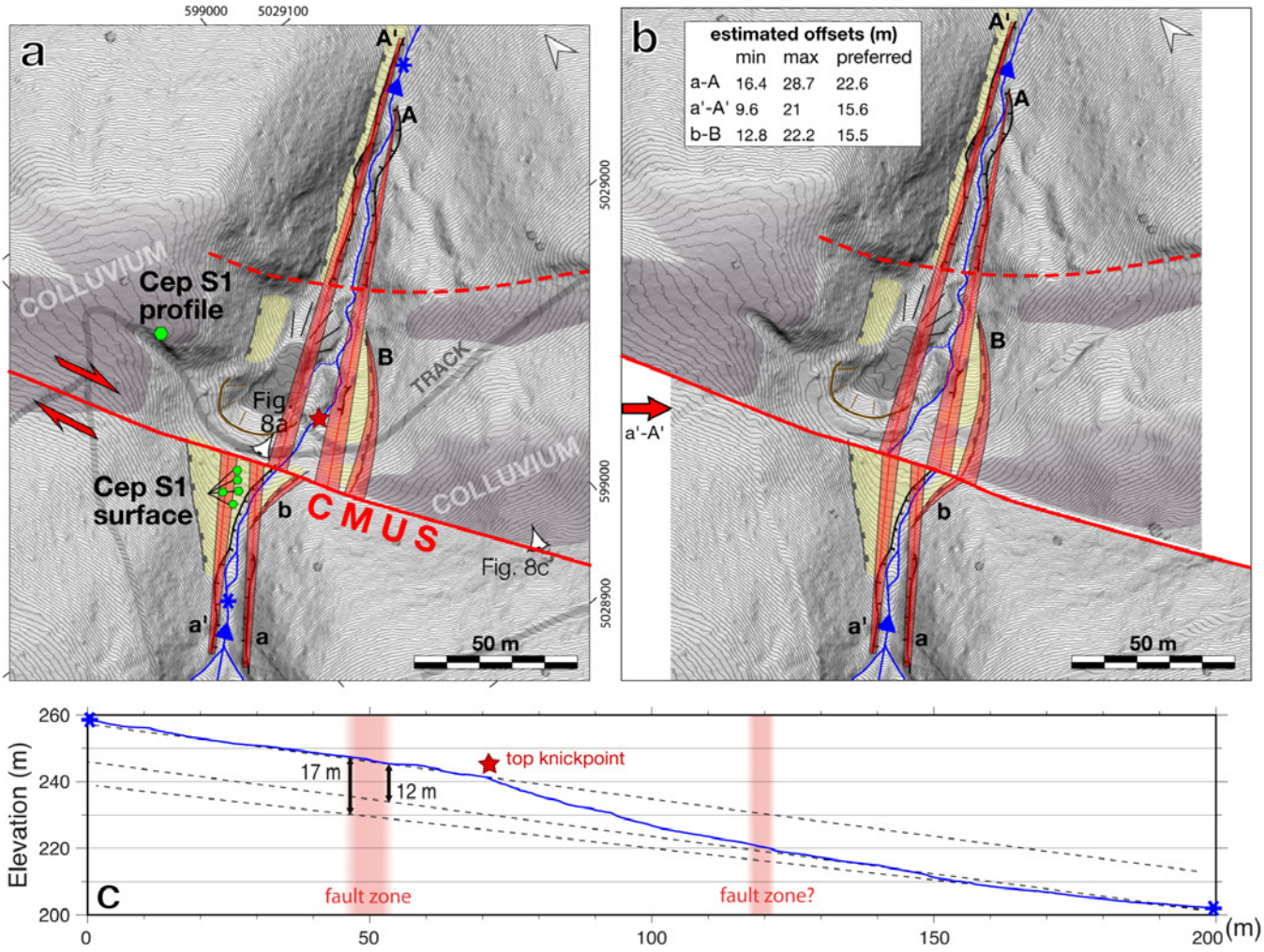

Figure 6 – Offset markers at the Cepeliš site S1 on the CMUS from high-resolution shaded LiDAR DEM (50 cm contour line spacing) and longitudinal profile along the stream (between asterisks). The morphotectonic interpretation shown in map a is used for back-slipping estimations shown in b. Terrace outer risers are shown with black lines and thin tick marks and inner risers by gray lines and thick tick marks. 3 set of piercing lines were analyzed to reconstruct plausible offsets along the CMUS. Their minimum, maximum and preferred estimates are shown in the table of the panel B, and represented by triangular-shaped transparent red polygons (for the minimum and maximum piercing lines axis) and a thin red line to show the preferred orientation of the markers. Back-slipping of offset markers a'-A' (outer risers of the left-bank terraces in yellow) gives a preferred displacement of 15.6 m. The gray area on the left-bank of the stream is a man-made surface. The green hexagons indicate the Cep_S1 depth-profile (Cep_S1_6 to Cep_S1_12) and surface samples (Cep_S1_1 to Cep_S1_5) used for cosmogenic dating. The longitudinal profile in c shows a large knickpoint of 12 m to 17 m-high downstream from the main fault trace. A version of the figure free of interpretations is shown in Figure S1 (Supporting Information).

On both sides of the stream, an abandoned alluvial terrace is preserved upstream of the main fault and downstream of the main fault as well as on the left-bank downstream of the secondary fault (yellow surfaces in the Figure 6a, Figure S1). The upper one is less incised (<50 cm) than the lower one (1-2 m), but they likely belong to the same depositional event if we consider that they are located on both sides of the knickpoint. Unfortunately, their continuity on the left-bank is prevented by an anthropized area, now corresponding to a pumped spring, potentially associated to a former landslide. The outer terrace risers or the related flank incision when the terrace is missing are relatively well preserved upstream from the main fault and downstream of the secondary fault, while the inner terrace incision is disturbed on the left-bank of the main fault downstream.

We estimate the cumulative offset of the drainage and its terraces assuming that most of the deformation occurs on the main fault strand, but we cannot exclude that the potential secondary fault accommodates part of the slip as well. To determine the offset range at this site we use the extrapolation of three sets of piercing lines from markers assumed to be of similar ages (Figure 6a): 1) a-A corresponds to the outer risers on the right-bank, extrapolated form the far-field, 2) a'-A' corresponds to the outer risers on the left-bank, extrapolated form the far-field, and 3) b-B uses the near-field inner riser. For each piercing-lines we provide a range of plausible orientations of the geomorphological marker (confined in the light transparent red polygon), and a preferred piercing-line axis (thin red line within the polygon). By projecting these piercing-lines onto the fault, we can quantify the lateral offsets with a minimum, a maximum

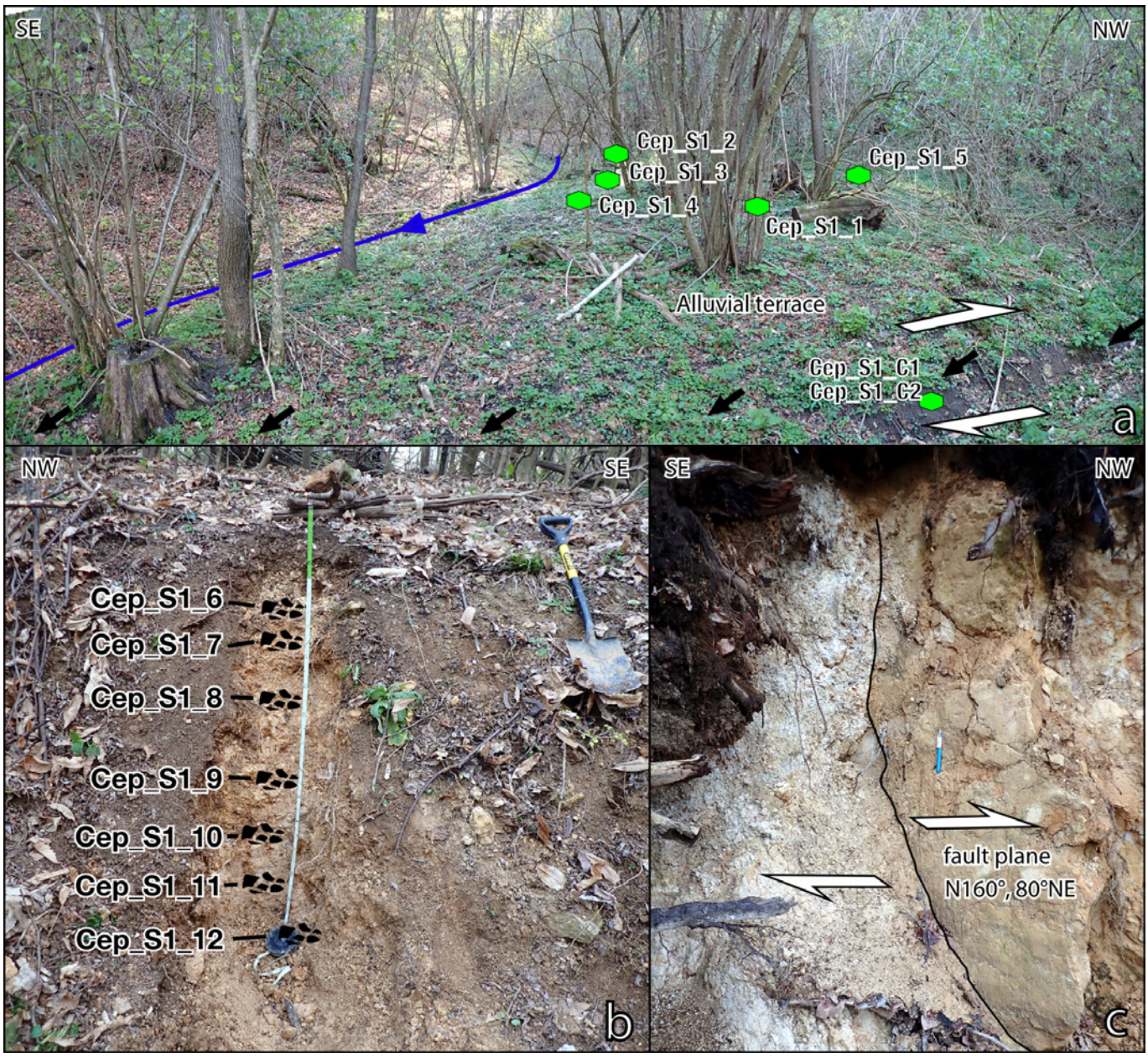

Figure 7 – Field photographs from Cepeliš site S1 on the CMUS. In a, the sampled alluvial surfaces and the inferred fault trace offsetting the drainage from Figure 6. 5 cosmogenic samples were collected from this surface (Cep_S1_1 to Cep_S1_5) sampling embedded large pebbles, and 2 radiocarbon samples (Cep_S1_C1 and Cep_S1_C2) along the refreshed scarp along the track. In b), the cosmogenic depth-profile within the colluvium from the left-bank hillside (Cep_S1_6 to Cep_S1_12). In c), a fault plane with a strike azimuth of 160° and a dip angle of 80° toward the NE exposes the Middle Miocene calcarenites (Badenian).

and a preferred estimate (Figure 6b): 1) [16.4 – 28.7] m with a preferred estimate of 22.6 m, 2) [9.6 - 21] m with a preferred estimate of 15.6 m, and 3) [12.8 – 22.2] m with a preferred estimate of 15.5 m. Considering that the inner riser formation should precede the one of the outer riser due to a later incision phase, we note that our measurements does not show a higher cumulative offset of the inner risers b and B relative to the outer risers (a-A and a'-A'), but the large uncertainties on the offset range likely prevent a precise comparison of these estimates.

4.1.2 Cepeliš S2a – NW-site on the CMUS

The Cepeliš S2a site is located at the NW edge of the CMUS striking ~N153°, just before its junction with the down-hill CMLS (Figures 5, 8, and 9, Figure S2). The fault can easily be traced from the Cepeliš S1 site (located 240 m to the SE), but quickly disappears within the deeply incised stream, likely because of the active erosion of the canyon flanks (dipping 45° to 50°) and of the hill's front. Indeed, numerous landslides are observed in the gorge, in particular on the left-bank of the stream where the landslide scars reach the ridge crest.

The canyon is straight and ~50 m deep where it is expected to cross the CMUS (Figure 8a), whereas a right-lateral offset is preserved in the continuity of the upper fault strand (Figures 8a and 10a). Downstream, a 20-40 m wide alluvial terrace is abandoned on the right-bank of the stream (Figure 10c), approximately

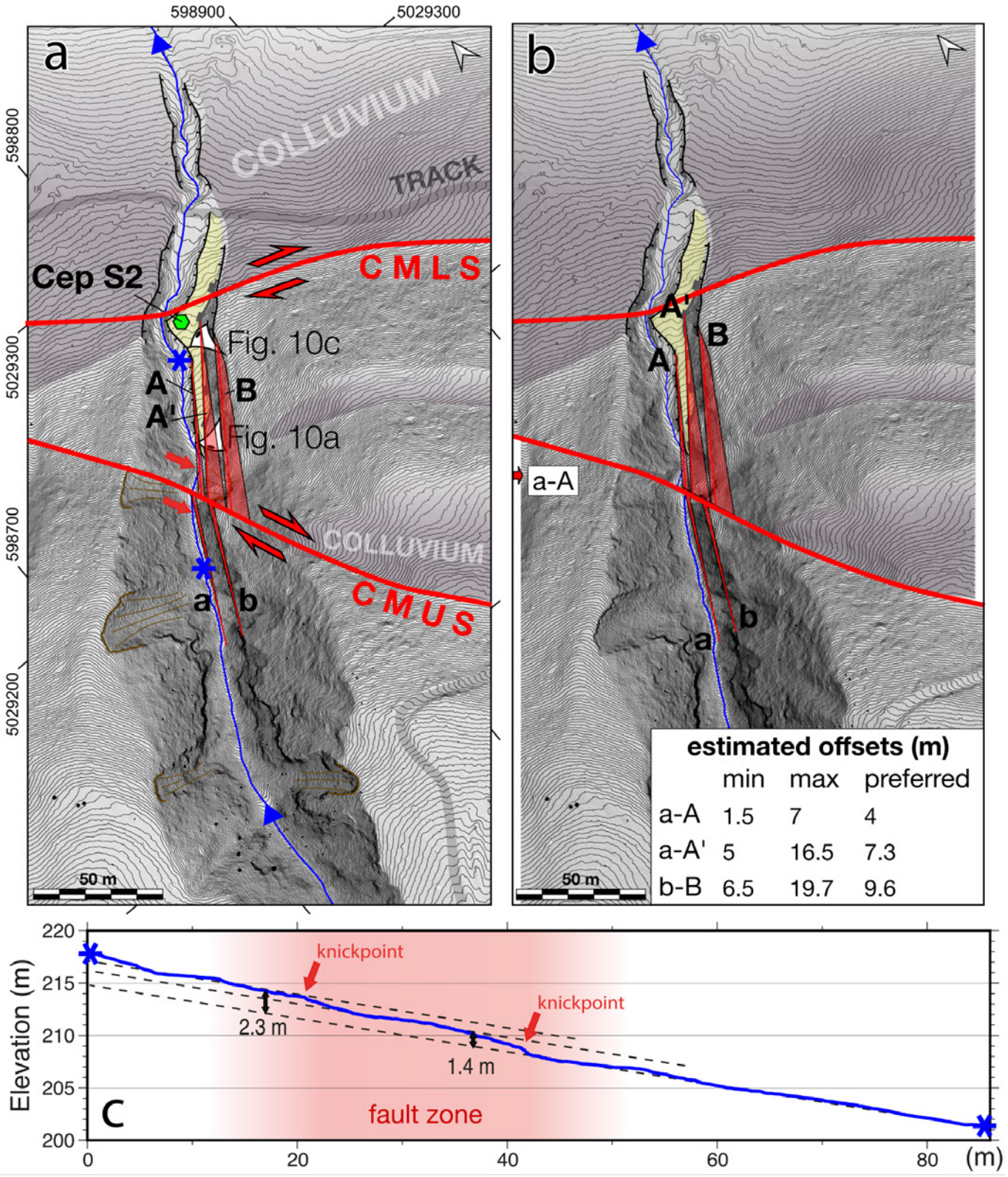

Figure 8 – Offset markers at the Cepeliš site S2a on the CMUS from high-resolution shaded LiDAR DEM (50 cm contour line spacing) and longitudinal profile along the stream (between asterisks). The morphotectonic interpretation shown in map a is used for back-slipping estimations shown in b. Terrace outer risers are shown with black lines and thin tick marks and inner risers by gray lines and thick tick marks. 3 set of piercing lines were analyzed to reconstruct plausible offsets along the CMUS. Their minimum, maximum and preferred estimates are shown in the table of the panel B, and represented by triangular-shaped transparent red polygons (for the minimum and maximum piercing lines axis) and a thin red line to show the preferred orientation of the markers. Back-slipping of offset markers a-A (outer risers of the rigth-bank terraces in yellow) gives a preferred displacement of 4 m. The purple hexagon indicates the Cep_S2 surface samples (Cep_S2_1 to Cep_S2_3) used for cosmogenic dating. The longitudinal profile in c shows a series of knickpoints within the fault zone reaching a cumulative height of 2.3 m. A version of the figure free of interpretations is shown in Figure S2 (Supporting Information).

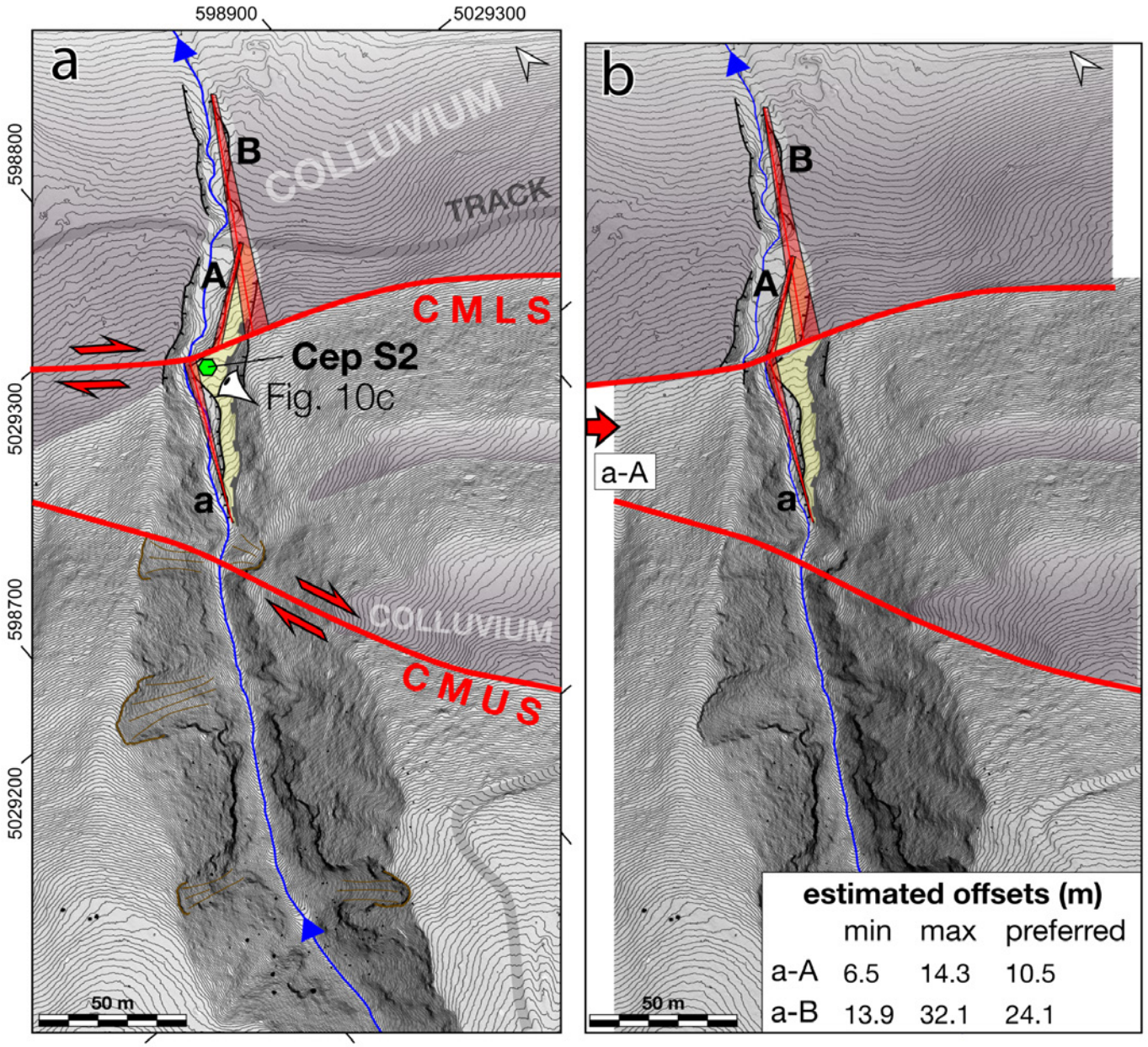

Figure 9 – Offset markers at the Cepeliš site S2b on the CMLS from high-resolution shaded LiDAR DEM (50 cm contour line spacing) and longitudinal profile along the stream (between asterisks). The morphotectonic interpretation shown in map a is used for back-slipping estimations shown in b. Terrace outer risers are shown with black lines and thin tick marks and inner risers by gray lines and thick tick marks. 2 set of piercing lines were analyzed to reconstruct plausible offsets along the CMLS. Their minimum, maximum and preferred estimates are shown in the table of the panel B, and represented by triangular-shaped transparent red polygons (for the minimum and maximum piercing lines axis) and a thin red line to show the preferred orientation of the markers. Back-slipping of offset markers a-A (outer risers of the right-bank terraces in yellow) gives a preferred displacement of 10.5 m. The purple hexagon indicates the Cep_S2 surface samples (Cep_S2_1 to Cep_S2_3) used for cosmogenic dating. A version of the figure free of interpretations is shown in Figure S3 (Supporting Information).

2.5 m above the current seasonal stream. The slope of the terrace is ~9.5°, slightly lower than the one derived from the current stream bed (~11.5°). Analyzing the topographic profile of the stream crossing the fault zone, we note that two small knickpoints, 1.4 m and 0.9 m high, fit the position of the potential fault stepover across the canyon (Figure 8c). As no significant lithological contrast is mapped here in the Badenian limestone, such knickpoints might sign a small dip-slip component of the fault zone (~2.3 m).

Although a terrace riser is relatively well preserved downstream, the lack of corresponding terraces levels upstream complicates the use of its inner and outer risers as piercing lines. To estimate the cumulative offset on this strand we used the right-bank of the stream with two hypotheses (Figure 8a) where the outer riser of the actual flood plain upstream (piercing line a) have been aligned to the terrace outer riser (piercing line A) or its inner riser (piercing line A') downstream. These two hypotheses provide fault offset of [1.5 - 7] m with a preferred estimate of 4 m for piercing-lines a-A, and of [5 – 16.5] m with a preferred estimate of 7.3 m for

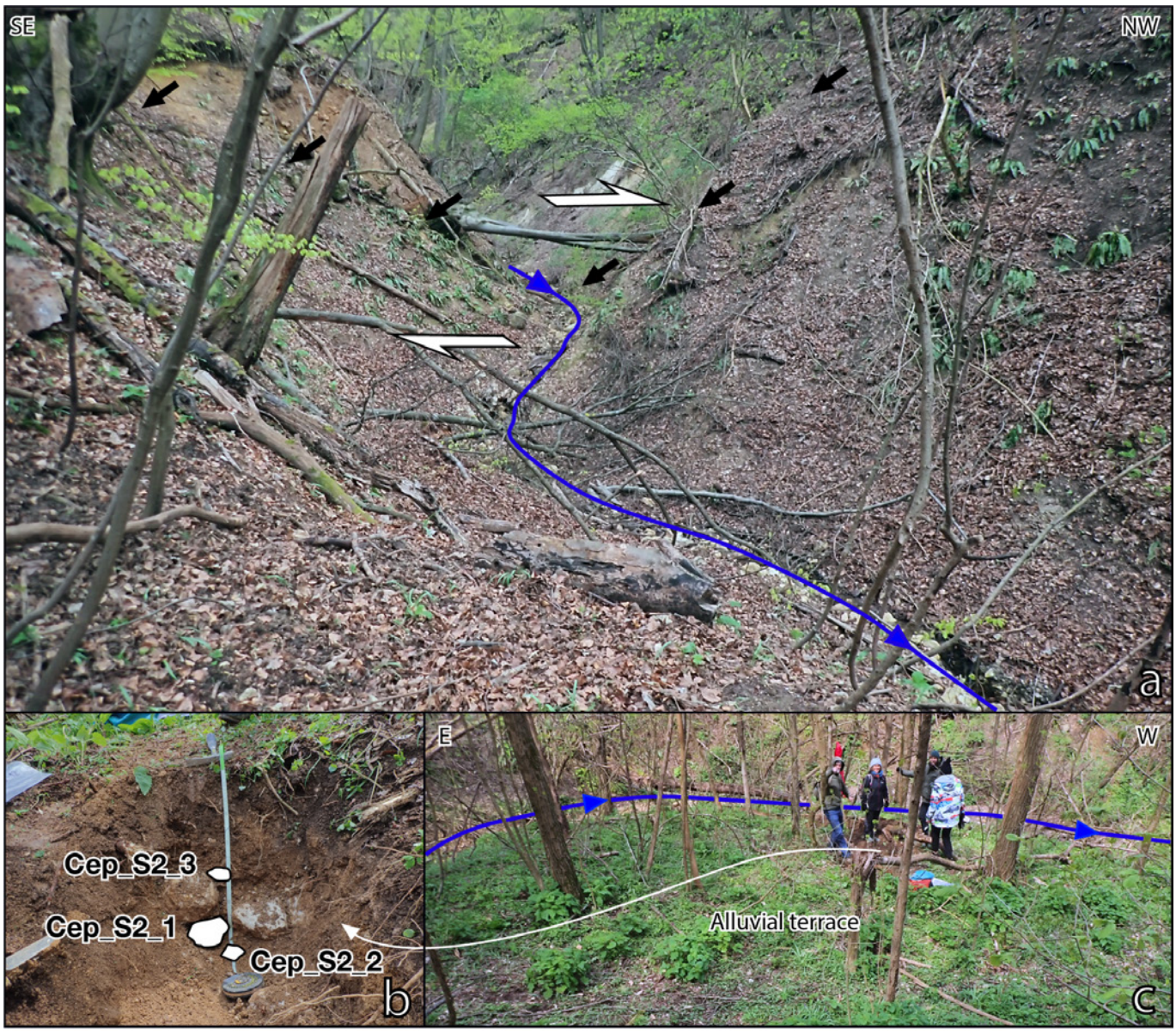

Figure 10 – Field photographs from Cepeliš site S2 between the CMUS and the CMLS. In a) the offset stream and the fault trace. The alluvial terrace downstream shown in b is sampled for cosmogenic dating from a hand-made pit at the subsurface (c). The 3 cosmogenic samples are Badenian pebbles located between 40-70 cm depth.

piercing-lines a-A'. The inner and outer risers A' and A should enclose the age of the terrace formation, and therefore the offset of the outer riser (a-A) should be smaller than the one of the inner riser (a-A'), which seems to be the case here. We also note that a former incision scarp follows the right-bank of the canyon 10 to 20 m above the stream bed upstream and downstream of the fault respectively. This scarp might be related to the former and older incision phase preceding the formation of the terrace, which is consistent with its larger offset (piercing lines b and B) of [6.5 – 19.7] m with a preferred estimate of 9.6 m compared to the offsets of the piercing lines a-A and a-A'.

4.1.3 Cepeliš S2b – NW-site on the CMLS

The Cepeliš S2b site is located on the CMLS, ~100 m to the NE downstream from the Cepeliš S2a site on the termination of the CMUS. The CMLS marks here the transition between the deeply incised canyon and the smoother reliefs at the base of the Hrastovica hillside (Figure 9a, Figure S3). The stream incises downstream from the fault within the colluvium and slope wash deposits and shows a right-lateral offset along-strike. The alluvial terrace used to estimate the offset on the CMUS upstream (site Cepeliš S2a) is on this site intersected downstream by the CMLS fault, which provides another set of piercing lines to determine a range of offsets on the CMLS.

To estimate the cumulative offset on this strand we also use the right-bank of the stream with three hypotheses (Figure 9a): 1) the outer riser of the terrace upstream and downstream of the fault is offset (piercing lines a-A), 2) the outer riser of the terrace upstream is offset relative to the outer riser in the far-field downstream of the fault (piercing lines a-B), and 3) the inner riser of the terrace upstream from the fault is offset relative to the outer riser in the far-field downstream

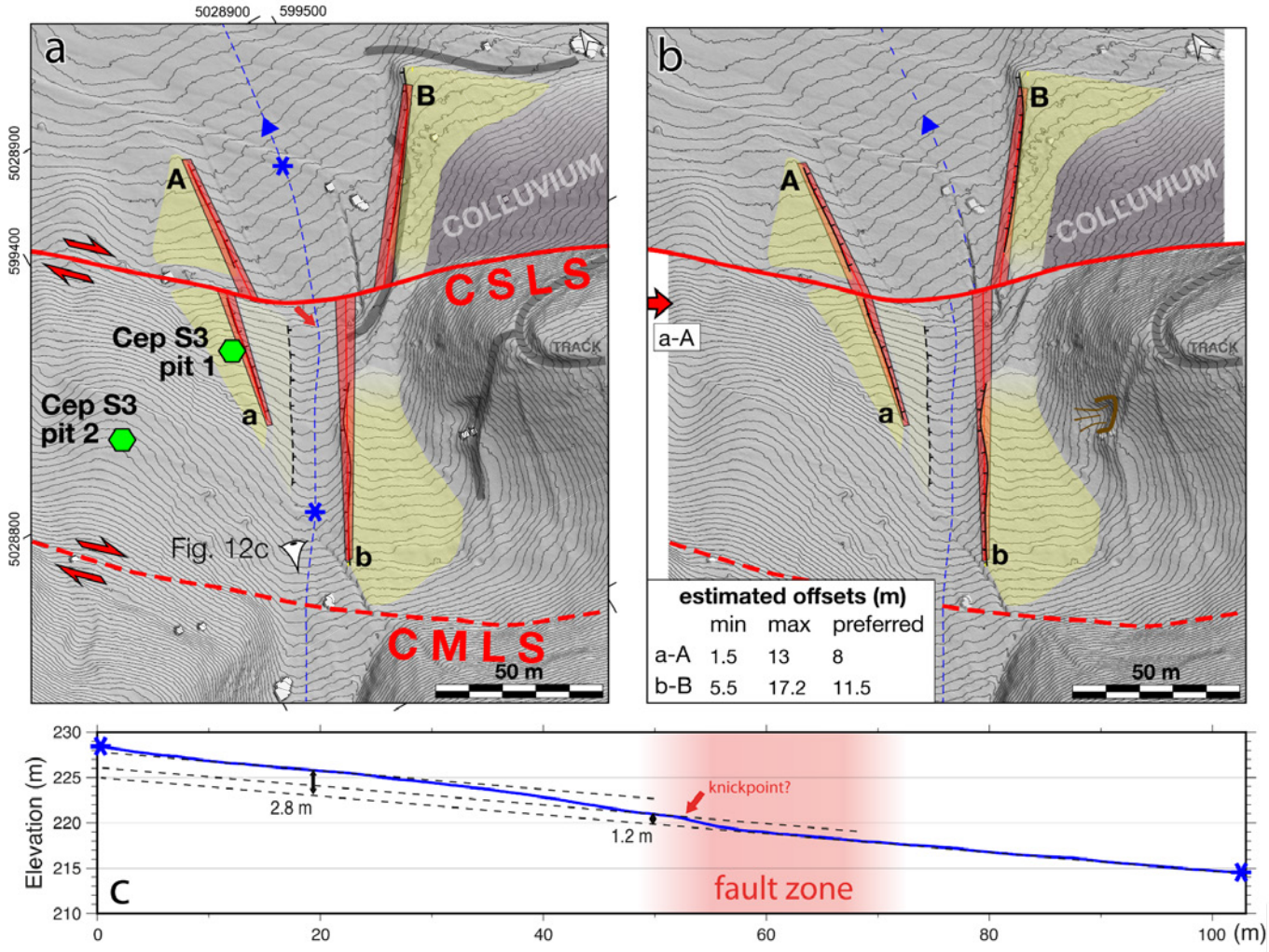

Figure 11 – Offset markers at the Cepeliš site S3 on the CSLS from high-resolution shaded LiDAR DEM (50 cm contour line spacing) and longitudinal profile along the stream (between asterisks). The morphotectonic interpretation shown in map a is used for back-slipping estimations shown in b. Terrace outer risers are shown with black lines and thin tick marks and inner risers by gray lines and thick tick marks. 2 set of piercing lines were analyzed to reconstruct plausible offsets along the CMLS. Their minimum, maximum and preferred estimates are shown in the table of the panel B, and represented by triangular-shaped transparent red polygons (for the minimum and maximum piercing lines axis) and a thin red line to show the preferred orientation of the markers. Back-slipping of offset markers a-A (outer risers of the left-bank terraces in yellow) gives a preferred displacement of 8 m. The purple hexagons indicate the Cep_S3 cosmogenic (Cep_S3_1 to Cep_S3_3 in pit 1) and radiocarbon samples (Cep_S3_C1 to Cep_S3_C3 in pit 1 and Cep_S3_C4 to Cep_S3_C5 in pit 2) used for dating. The longitudinal profile in c shows a knickpoint of 1.2 m to 2.8 m. A version of the figure free of interpretations is shown in Figure S3 (Supporting Information).

of the fault (piercing lines a'-B). By projecting these piercing-lines onto the CMLS, we found [6.5 – 14.3] m with a preferred estimate of 10.5 m for the set of piercing lines a-A, [13.9 – 32.1] m with a preferred estimate of 24.1 m for the piercing lines a-B.

4.1.4 Cepeliš S3 – Site on the CSLS

The Cepeliš S3 site is located on the lowest fault strand, striking ~N120° (CSLS, Figures 5 and 11). The fault runs here at the base of the Hrastovica hillside along the incision outlets (Figure 12a). A second strand belonging to the CMLS is located ~80 m to the SW but no measurable offset was found along this fault section. The valley is relatively wide and incise within a smooth topography, which allowed the formation and preservation of an alluvial fan apex on both sides of the stream (yellow polygons on Figure 11a and Figure S4). Indeed, the sedimentological analysis of the pit 1 and 2 on the left-bank of the stream revealed thick units of plastic clays at the surface. The origin of these clayey deposits is not well understood, but they could be related to the former Sava alluvial system that deposited low energy detrital material along the Hrastovica hills during the Plio-Quaternary, or it could be slope wash deposits of clayey units along the Hrastovica hillside.

The seasonal stream that incised the valley is poorly active now and we can barely reconstruct its position, in particular downstream the lower fault strand where it supplies a wide alluvial plain now occupied by agricultural land. Upstream, it should flow within a 10-15 wide flattened valley bounded by alluvial terraces. Here too the stream possibly crosses the fault in a relay zone as the two segments of the lower strand on each

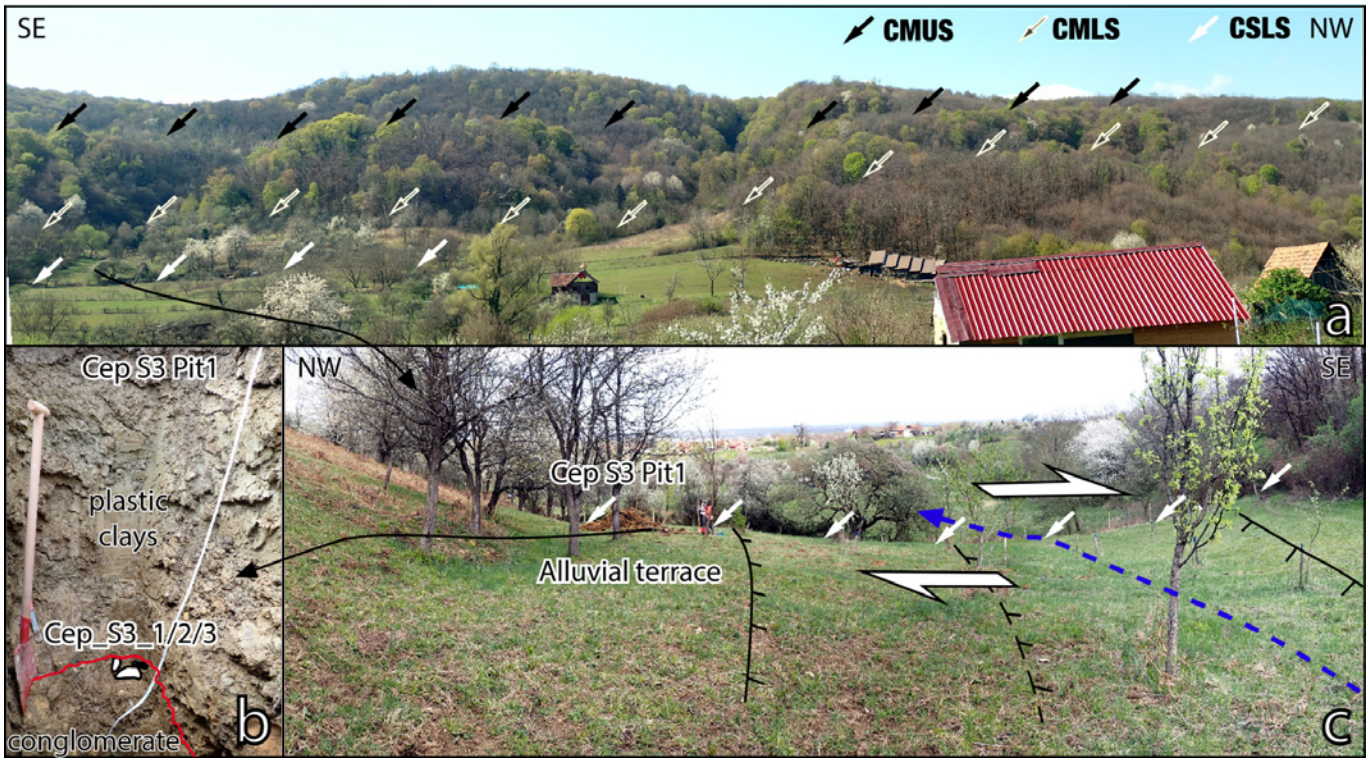

Figure 12 – Field photographs from Cepeliš site S3 on the CSLS. In a) a panoramic of the eastern side of the Hrastovica hills showing the CMUS (black arrows up-hill), the CMLS (gray arrows) and the CSLS (white arrows down-hill). In b and c, the 1.7 m deep pit 1 where cosmogenic (Cep_S3_1 to Cep_S3_3) and radiocarbon samples (Cep_S3_C1 to Cep_S3_C3) were collected from the basal conglomerate and overlying clays respectively.

side of the valley are not completely aligned (Figure 11a). Analyzing the river bed profile reveals here a 1.2 m to 2.8 m high knickpoint coinciding with the fault trace (Figure 11c). As the lithology is the same on both sides of the fault, we then assume that some dip-slip likely occurs on this strand too. This main level of terraces that seems to belong to the same erosional event is 1.2-1.5 m above the valley floor upstream from the fault, and about 1 to 2 m downstream. Another small terrace on the left-bank of the valley upstream overcomes the valley floor of about 0.5 m and might correspond to a younger erosive phase (Figure 11a).

The terrace risers are preserved up to the fault along the left-bank, while the risers from the right-bank of the stream is disturbed by a track for ~30 m across the fault. We use the outer risers from the left-bank and right-bank (piercing lines a-A and b-B respectively) that gives offset of [1.5 - 13] m with a preferred estimate of 8 m (a-A) and of [5.5 – 17.2] m with a preferred estimate of 11.5 m (b-B).

4.2 Gornja Budičina site on the DBSPF

The Donja Budičina section corresponds to the southeastern section of the Donja Budičina Southern Petrinja Fault (DBSPF, Figure 3 and Figure 12), a portion of the Petrinja Fault without surface ruptures from the 2020 Petrinja earthquake (*Baize et al.*, 2022). The long-term fault trace mostly follows the NE side of the Hrastovica hills (Figure 3 and Figure 13). As for the Cepeliš area, a river sub-parallel to the fault drains toward the NW the small seasonal catchments that flow across the NE slope of the Hrastovica hills up to the Petrinjčica river. The section is divided in two distinct zones separated by the Vražji Skok river. To the NW, the transition from the top of the Hrastovica hills to the valley is narrow, characterized by deep incisions and a strong topographic gradient (~24°). To the SE, the transition zone is smoother (mean slope of ~16°) and shows a staircase morphology similar to the Cepeliš site, with incised streams and strong topographic gradients hill-ward and wider channels and lower topographic gradients basin-ward (Figure 13). The lithology at the bottom of the hill is mostly made of weak Upper Miocene sediments from the Pannonian phase, at the origin of shallowly incised, U-shaped valleys, while uphill the streams incise the stronger Lower Miocene units creating deeper and narrower V-shaped valleys. According to the geological map, the morphotectonic trace fits well this tectonic contact between the lower and Upper Miocene units (*Pikija*, 1987). To the NW, such geological contact is mostly buried by the numerous alluvial fans and slope wash deposits that formed at the outlet of the incised streams. Although the fault trace seems straighter to the NW, the geomorphological record of datable cumulative offsets is limited, this is why we focused our analysis on the southern portion of the fault near Gornja Budičina (Figure 14) where alluvial terraces are preserved.

Gornja Budičina site

The Gornja Budičina site is located on the lower branch of the fault ~100 m from the steep topographic front. In this part, we also mapped a secondary branch (Figures 3 and 13) that likely splits the main fault

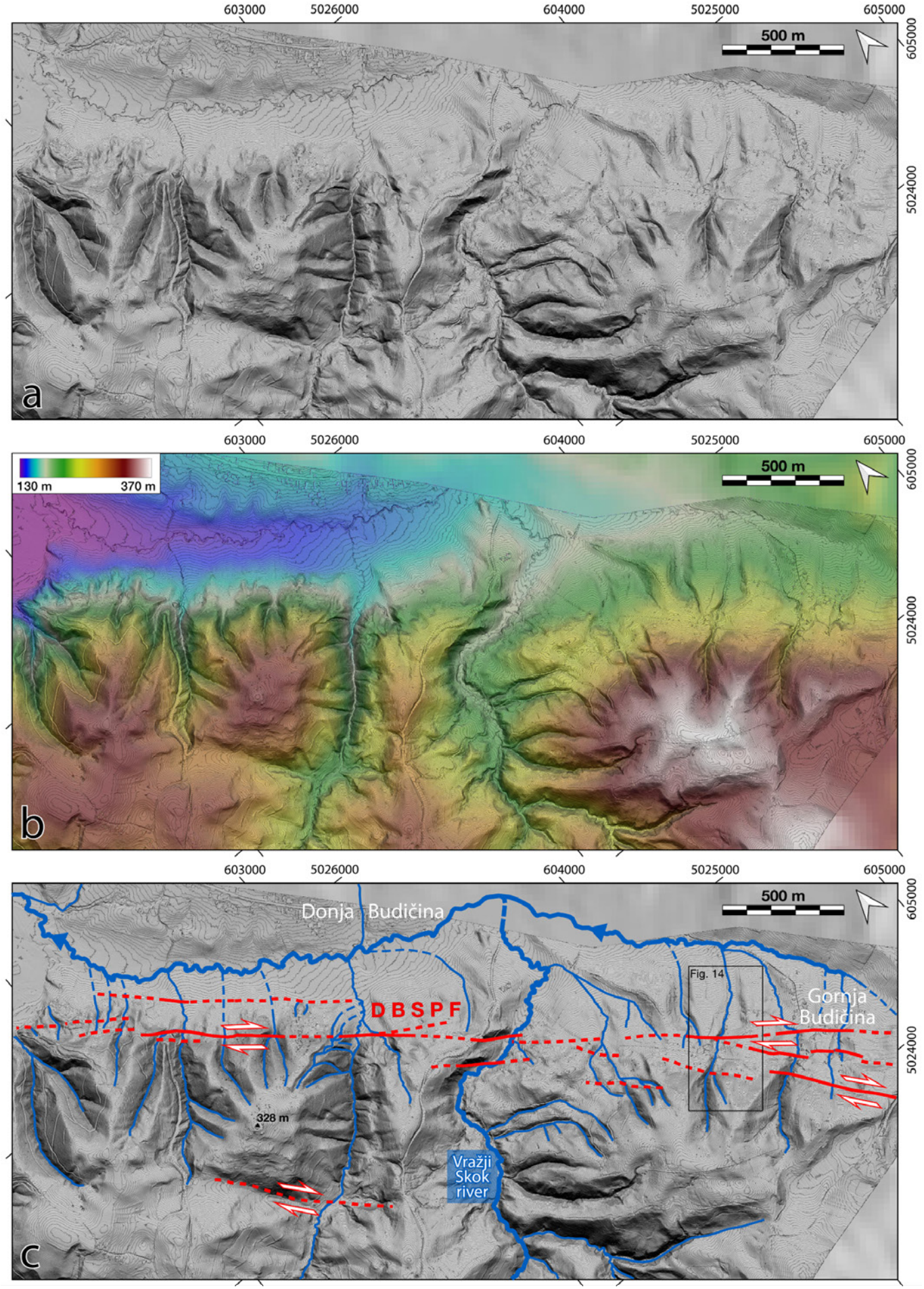
603000
5026000
604000
5025000
605000
605000
5024000
500 m
a
130 m
370 m
b
Donja Budičina
DBSPF
Fig. 14
Gornja Budičina
328 m
Vražji Skok river
c

Figure 13 – Morphotectonic map showing the fault trace along the Donja Budičina section of the Southern Petrinja Fault (DBSPF). The spacing between the contour lines draped on the shaded relief maps is 1 m. The black rectangle shows the location of the Gornja Budičina site where displaced geomorphic markers are quantified in Figure 14. The lithology at the bottom of the hill is mostly made of weak Upper Miocene sediments from the Pannonian phase, at the origin of shallowly incised, U-shaped valleys, while uphill the streams incise the stronger Lower Miocene units creating deeper and narrower V-shaped valleys.

strand in two strands when crossing the incised stream (Figure 14a and Figure S5). The local stream shows a right-lateral offset aligned on the main fault and the topographic profile along the river bed reveals one or two knickpoints that we relate to the fault activity (Figure 14c). The first knickpoint likely coincides with the fault zone and is about 1.6 m high. A second one is located 50 m upstream but it is unclear whether this knickpoint is due to a track crossing the river. At a larger scale, we note, however, that the total vertical component reaches ~3.1 m. There are two possible explanations for this knickpoint zone: either it is of tectonic origin, or it is a consequence of an upstream regressive erosion mostly efficient in the Lower Miocene units and slowed down in the Upper Miocene units (the absence of outcrops makes it impossible to conclude with certainty here).

The drainage in the fault zone area incised a narrow ~10 m deep canyon which enlarges downstream to a 80 m wide valley likely as a consequence of cumulated right-lateral offset (Figure 14a). A set of alluvial terraces is preserved on both sides of the stream, about 2-3 m above the river bed upstream and 1.2-2.5 m downstream. The river bed slopes downstream ~6.9°, that is relatively close to the slope of the abandoned terrace on its right-bank that is 7.3°. The upstream terrace risers are shorter and less preserved than their downstream equivalent but they are reliable enough to be used as piercing lines. We use outer risers on the left-bank (piercing lines a-A) and the right-bank (piercing lines b-B) to quantify the cumulative offset associated to the abandonment of the yellow terrace. The estimated offset ranges from [1.7 – 29.2] m with a preferred estimate of 21.5 m for the piercing lines a-A, and [10 – 25.2] m with a preferred value of 17.3 m for the piercing lines b-B (Figure 14b). We can also consider the right-bank lateral border of the former incision that led to the terrace formation, characterized by the piercing lines c-C, which gives a cumulative offset of [75.5 – 121] m with a preferred estimate of 107 m. Nevertheless, this incision largely precedes the formation of the terrace, that is why the estimated offset is much larger than the one derived from the outer risers of the terrace.

5 Quaternary Dating of Displaced Markers

5.1 Sampling Strategy

To determine a slip-rate from the estimated cumulative offsets we sampled abandoned surfaces associated with the deformation for cosmogenic radionuclide dating and radiocarbon dating. Where possible, we sought to collect cosmogenic samples on a depth profile to retrieve both the exposure time and the denudation rate affecting the surface (Braucher et al., 2009). When it was too challenging to dig a profile by hand, or when the thickness of the deposits was insufficient to make a depth profile, we only collected 3-5 samples at the surface or at depth to estimate the exposure time assuming an a priori denudation rate constraint. Because Badenian limestones from the Hrastovica hills composes most of the pebbles and clasts from the abandoned surfaces, we analyzed the ^{36}Cl radionuclide that is produced by reactions of cosmic rays with the Ca constituting carbonates. Charcoals were collected to complement cosmogenic samples, or where no coarse detrital deposits were found.

5.2 Quaternary Dating Methodology

5.2.1 Exposure Dating

^{36}Cl dating methodology

The exposure ages were determined by measuring the concentration of [^{36}Cl] produced in situ. The samples are either pebbles or clasts, and, depending on their size, we collected a single piece or an amalgam of smaller fragments to obtain sufficient material for concentration measurements. After crushing the sample, we used the 250–1000 m fraction that is leached and then dissolved following the method from Stone et al. (1996) and modified by Schlagenhauf et al. (2011). Each dissolved sample is spiked with a known quantity of isotopically enriched stable chloride carrier to allow the determination of [Cl] and [^{36}Cl] by isotope dilution (*Schlagenhauf et al.*, 2011). The Cl is then precipitated as AgCl and the ^{36}Cl/^{35}Cl and ^{35}Cl/^{37}Cl ratios are both measured with the French accelerator mass spectrometer (AMS) national facility ASTER (Accélérateur pour les Sciences de la Terre, Environnement, Risques), located at CEREGE in Aix-en-Provence. Those ratios are normalized by a standard with a ^{36}Cl/^{35}Cl value of $(1.428 \pm 0.015) \times 10^{-12}$ (Merchel et al., 2011) and assuming a natural ^{35}Cl/^{37}Cl ratio of 3.127. Ca concentrations of each sample were measured by inductively coupled plasma atomic emission spectrometry (ICP-AES) at CEREGE (Table 1).

The ^{36}Cl half-life is 3.014×10^5 years which corresponds to a decay constant of $(2.303 \pm 0.016)\ 10^{-6}$ yr^{-1}. The counting statistics, machine stability and blank correction are integrated in the analytical uncertainties. The spallation production rate from Ca is 42.2 ± 4.8 atoms ^{36}Cl $(g \cdot Ca)^{-1} \cdot yr^{-1}$ (*Schimmelpfennig et al.*, 2011), normalized to sea level and high latitude using the scaling method of *Stone* (2000). We used a rate of 696 ± 185 $n \cdot cm^{-2} \cdot a^{-1}$ for the production of epithermal neutrons from fast neutrons at the base of the atmosphere (*Marrero et al.*, 2016)

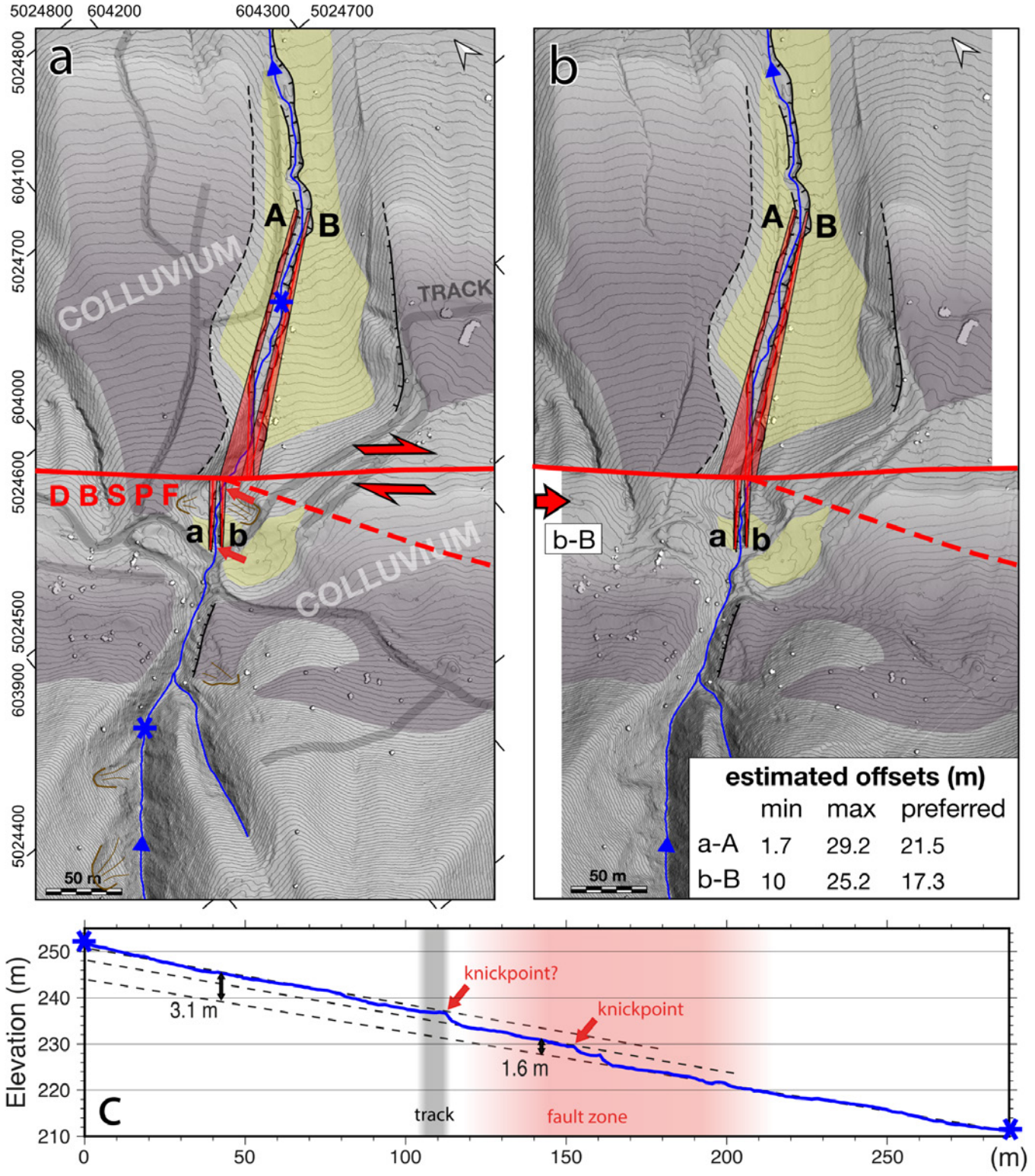

Figure 14 – Offset markers at Gornja Budičina on the DBSPF from high-resolution shaded LiDAR DEM (50 cm contour line spacing) and longitudinal profile along the stream (between asterisks). The morphotectonic interpretation shown in map a is used for back-slipping estimations shown in b. 2 set of piercing lines were analyzed to reconstruct plausible offsets along the DBSPF. Their minimum, maximum and preferred estimates are shown in the table of the panel B, and represented by triangular-shaped transparent red polygons (for the minimum and maximum piercing lines axis) and a thin red line to show the preferred orientation of the markers. Back-slipping of offset markers b-B (outer risers of the right-bank terraces in yellow) gives a preferred displacement of 17.3 m. The longitudinal profile in c shows a knickpoint within the fault zone of 1.6 m, and potentially up to 3.1 m considering the far-field upstream stream axis. A version of the figure free of interpretations is shown in Figure S3 (Supporting Information).

Table 1 – Sample information, AMS measurements, calculated ^{36}Cl, chlorine and Ca concentrations and estimated exposure ages following the approach from *Schimmelpfennig et al.* (2009). The shielding factor was estimated in the field with a compass. The reported analytical uncertainties include uncertainties in the isotopic ratios of the standards, on the blank chemical measurements and in AMS counting statistics and an external AMS error of 0.5% (*Arnold et al.*, 2010) plus the uncertainties associated with the ^{36}Cl nuclide half-lives. The full chemical composition (major and traces elements) of underlined samples (fraction <250 μm) was analyzed at the Service d'Analyse des Roches et des Minéraux (SARM) and given in the Table S1.

Site	Sample	Lat. (°N)	Lon. (°E)	Elev. (m)	Sample depth (cm)	Shielding factor	^{36}Cl/^{5}Cl (x10^{-14})	^{35}Cl/^{37}Cl	^{36}Cl (x10^{4} atoms/g)	Cl (ppm)	CaO (%)	Denudation (mm/kyr) Calculated for t = ∞	CRE age (kyr) Denudation = 0 mm/kyr	CRE age (kyr) Denudation = 30 mm/kyr
Cepeliš site S1														
surface														
	Cep_S1_1	45.4075	16.2641	247	5	0.965	44.79	16.160	24.488 ± 1.084	7.74	55.4	161,13	10.49 ± 1.30	13.24 ± 1.64
	Cep_S1_2	45.4075	16.2641	247	5	0.965	18.98	18.671	9.275 ± 0.456	5.95	54.3	437.20	4.03 ± 0.50	4.36 ± 0.55
	Cep_S1_3	45.4075	16.2641	247	5	0.965	12.95	24.316	7.144 ± 0.384	5.03	54.3	574,27	3.07 ± 0.39	3.27 ± 0.42
	Cep_S1_4	45.4075	16.2641	247	5	0.965	20.53	22.783	9.559 ± 0.455	4.54	54.5	422.11	4.16 ± 0.52	4.52 ± 0.57
	Cep_S1_5	45.4075	16.2641	247	5	0.965	10.52	29.128	44.188 ± 1.886	3.08	54.6	82.66	19.8 ± 2.49	34.30 ± 4.32
profile														
	Cep_S1_6	45.4079	16.2642	253	25	0.992	42.78	20.155	23.118 ± 1.099	6.02	53.4	//	11.65 ± 1.21	14.98 ± 2.66
	Cep_S1_7	45.4079	16.2642	253	35	0.992	35.50	23.453	21.823 ± 1.010	5.79	53.4	//	//	//
	Cep_S1_8	45.4079	16.2642	253	55	0.992	34.71	20.344	19.975 ± 0.917	6.35	53.1	//	//	//
	Cep_S1_9	45.4079	16.2642	253	85	0.992	30.36	21.067	17.612 ± 0.811	6.16	52.9	//	//	//
	Cep_S1_10	45.4079	16.2642	253	105	0.992	31.81	18.905	17.665 ± 0.816	6.64	52.6	//	//	//
	Cep_S1_11	45.4079	16.2642	253	125	0.992	24.24	21.336	18.218 ± 1.057	7.88	52.7	//	//	//
	Cep_S1_12	45.4079	16.2642	253	145	0.992	24.84	20.244	15.455 ± 0.719	6.91	52.9	//	//	//
Cepeliš site S2														
	Cep_S2_1	45.4099	16.2627	201	55	0.976	7.335	14.840	4.761 ± 0.319	10.09	56.3	666,56	3.88 ± 0.54	4.14 ± 0.58
	Cep_S2_2	45.4099	16.2627	201	70	0.976	20.196	32.685	9.866 ± 0.418	3.17	56.4	296,47	9.49 ± 1.32	11.04 ± 1.54
	Cep_S2_3	45.4099	16.2627	201	35	0.976	22.395	23.698	11.816 ± 0.508	4.93	56.3	246,74	11.29 ± 1.57	13.55 ± 1.88
Cepeliš site S3														
	Cep_S3_1	45.059	16.2707	222	175	0,992	84.10	29.662	43.228 ± 2.141	3.69	54.2	41.53	Saturated	≫195.57 ± 45.30
	Cep_S3_2	45.059	16.2707	222	170	0,992	45.67	17.466	26.294 ± 1.214	7.50	53.5	77,21	53.47 ± 11.64	78.55 ± 17.10
	Cep_S3_3	45.059	16.2707	222	165	0,992	39.07	14.359	24.744 ± 1.179	10.19	53.3	83.31	49.80 ± 10.78	71.34 ± 15.44
Quarry														
	Q_1	45.4331	16.1817	220	490	0.855	39.476	8.962	23.371 ± 0.908	15.65	54.3	37.30	Saturated	≫264.34 ± 75.87
	Q_2	45.4331	16.1817	220	515	0.855	24.860	4.900	25.171 ± 1.147	49.82	54.3	34.63	Saturated	≫303.56 ± 83.28
	Q_3	45.4331	16.1817	220	545	0.855	25.644	5.595	21.213 ± 0.929	35.54	54.7	39.07	saturated	≫227.41 ± 62.76

and a neutron attenuation length of 160 $g \cdot cm^{-2}$. The full chemical composition (major and traces elements) of several crushed samples (fraction <250 m) was analyzed at the Service d'Analyse des Roches et des Minéraux (SARM) at Centre de Recherches Pétrographiques et Géochimiques (CRPG), Nancy (France) (samples Cep_S1_1, Cep_S1_2, Cep_S1_6, Cep_S1_12, Cep_S3_2 and Cep_S3_3, Table S1 in the Supporting Information). The assumed bulk rock density is 2.7 g cm^{-3} for every sample. We then used the Excel spreadsheet from *Schimmelpfennig et al.* (2009) to calculate the ^{36}Cl cosmic-ray exposure (CRE) based on the time-independent scaling functions from *Stone* (2000) (Table 1).

Denudation rates and steady state equilibrium

Usually, the calculated exposure ages must be considered only as minimum ages if the samples reached the steady state equilibrium, i.e., when the cosmogenic nuclide concentration depends only on the denudation rate because the production is balanced by the losses from the radioactive decay and the surface denudation (*Gosse and Phillips*, 2001). To test such a hypothesis, we determined the denudation rates corresponding to infinite exposure ages (Table 1). We found maximum denudation rates from 35 mm/kyr to 667 mm/kyr. Except samples Cep_S3_1, Q_1, Q_2 and Q_3 that have moderate denudation rates (35 mm/kyr to 42 mm/kyr) of the order of denudation rates in carbonate environments (~20-60 mm/ka; e.g., *Ryb et al.*, 2014; *Sadier et al.*, 2012; *Thomas et al.*, 2018) and thus likely saturated, the other ones are not at the steady state, and their concentration is used to determine the CRE age.

Depth profile modeling

The ^{36}Cl concentration along the depth profile depends on the surface denudation rate, the ^{36}Cl inheritance from each sample, the density of the deposit (controlling the attenuation), and the exposure duration. The concentration is modeled by varying these parameters (*Braucher et al.*, 2009), except the density that is fixed to 2.1 g cm^{-3} for the colluvium (Moulin et al., 2016) at the site Cepeliš S1. The best fit was determined by using a chi-square (^{2}) inversion (e.g., *Siame et al.*, 2004; *Braucher et al.*, 2009; *Moulin et al.*, 2016).

5.2.2 Radiocarbon Dating

Seven charcoals were collected from two 1.7 m deep pits at Cepeliš site S3 (Figures 11 and 12. The radiocarbon samples were graphitized and their ^{14}C concentration measured at the French ARTEMIS ^{14}C Accelerator Mass Spectrometer (AMS) facility (Saclay, France). The ^{14}C concentration is corrected from the fractionation with the 13C occurring both during sample preparation and the AMS measurement, calculated from the $^{13}C/^{12}C$ ratio, following the method from *Mook and van der Plicht* (1999). We then calibrate each radiocarbon age (Table 2) using OXCAL version 4.4.4 (*Ramsey*, 2009) and the Intcal20 calibration curve (*Reimer et al.*, 2020).

5.2.3 Quaternary Dating Results

To constrain the age of abandonment of the alluvial terrace from the site Cepeliš S1 we sampled the top of 5 boulders (>30 cm wide) embedded in the surface (Figures 6a and 7b). We were careful not to take blocks too close to the hillslope to avoid colluvial deposits, and away from the incision to prevent recent flood deposits. Nevertheless, the narrow width of this abandoned surface means that contamination by younger depositional events cannot be ruled out. The maximum denudation rates estimated for an infinite exposure time of these boulders range from 83 mm/kyr to 574 mm/kyr, that is clearly too high for such an environment, and thus those blocks are not at steady state. We first assess the exposure time assuming that the denudation is likely negligible (0 mm/kyr) for post-LGM terraces as proposed in the SW Balkan region (~5 mm/kyr, *Gromig et al.*, 2018; *Styllas et al.*, 2018). We then obtain ages from 3.07 ± 0.39 ka to 19.8 ± 2.49 ka (Table 1). Two charcoals extracted from this alluvial surface at shallow depth (~30 cm) were also dated and led to very young ages of 0-283 yr BP and 507-618 yr BP (Table 2).

We also sampled the colluvial deposits that cover the perched surface on the left-bank of the drainage at Cepeliš site S1 (Figure 7b). The exposure time is here estimated by modeling the depth profile constrained by 7 samples from 20 cm to 150 cm depth (Figure 15b). We first tested inversions with the denudation rate as a free parameter, but the results showed that the erosion was unconstrained. Thus, we tested a Monte Carlo inversion with a denudation rate of 0 mm/yr as an a priori constraint, inverting for the inherited concentration and the exposure duration. Our best model fits well the data if associated with an increase of inherited ^{36}Cl from 3.5 x 10^4 atoms/g to 7.5 x 10^4 atoms/g at depth, which represents 15.5% to 50% of the sample concentrations respectively. The best fitting model then gives an exposure duration of 11.65 ± 1.21 ka (Figure 15b and Table 1).

Cosmogenic dating has also been used to date the terrace abandonment downstream of the main fault strand at Cepeliš site S2. We were able to dig a 70 cm deep pit in the terrace away from the right-bank hillslope (Figures 8a, 10b and 10c). 3 samples were collected at a depth of 40-70 cm and we assume that they belong to the same unit corresponding to the last depositional events before the surface abandonment. The maximum denudation rates range here from 245 mm/yr to 667 mm/kyr, which also correspond to high values and thus confirm that the steady state is not reached. As for the surface samples of the site Cepeliš S1, we first assume that the denudation rate is negligible (0 mm/kyr), which gives ages from 3.88 ± 0.54 ka to 11.29 ± 1.57 ka (Table 1).

At the Cepeliš site S3, the same approach is used with 3 samples at the base of pit 1 dug within the alluvial terrace (Figures 11a, 12b and 12c). Two pebbles and an amalgam collected at 1.65 m depth were analyzed (Table 1). The sample Cep_S3_1 is likely saturated as we estimate a maximum denudation rate of ~42

Table 2 – Sample information, calculated ages from the ^{14}C concentration measured at the French ARTEMIS ^{14}C Accelerator Mass Spectrometer (AMS) and calibrated ages. The radiocarbon ages were calibrated using OXCAL version 4.4.4 (*Ramsey*, 2009) and the Intcal20 calibration curve (*Reimer et al.*, 2020).

Site	Sample	Lat. (°N)	Lon. (°E)	Elev. (m)	^{14}C age (years BP)	^{14}C age (calibrated)	^{14}C age (calibrated BP)
Cepeliš S1							
	Cep_S1_C1	45.4075	16.2641	247	170 ± 30	1667- >1941 AD	0-283
	Cep_S1_C2	45.4075	16.2641	247	515 ± 30	1332-1443 AD	507-618
Cepeliš S3							
Pit 1							
	Cep_S3_C1	45.059	16.2707	222	310 ± 30	1488-1647 AD	303-462
	Cep_S3_C2	45.059	16.2707	222	1055 ± 30	901-1029 AD	921-1049
	Cep_S3_C3	45.059	16.2707	222	23490 ± 180	25391-26037	25391-26037
Pit 2							
	Cep_S3_C4	45.4057	16.2701	234	7770 ± 50	6480-6696 BC	6480-6696
	Cep_S3_C5	45.4057	16.2701	234	12260 ± 70	12103-12839 BC	12103-12839

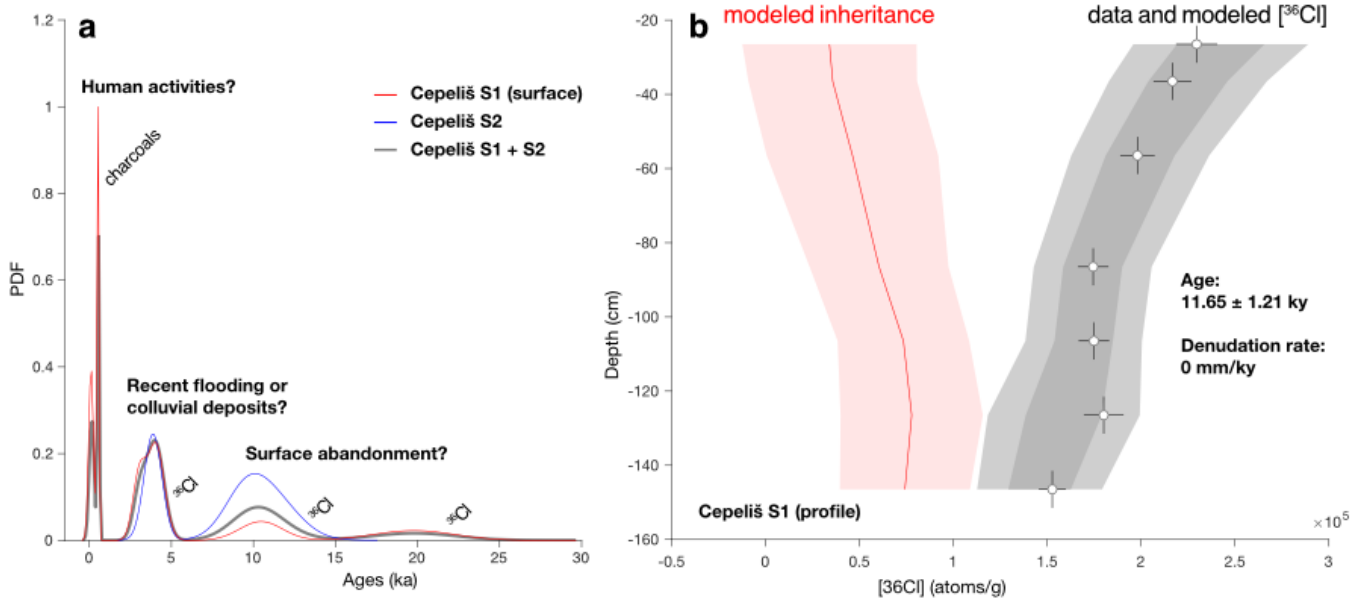

Figure 15 – Chronological constraints from Cepeliš site S1 and S2. Panel a: the probability density functions (PDF) of terrace ages considering the surface (site S1) and subsurface (site S2) ^{36}Cl CRE ages and radiocarbon ages from site S1. In red the distribution of ages from site S1, in blue from site S2 and in black the PDF with samples from both sites. Panel b: the cosmogenic depth-profile from the colluvium at the site S1 (shown in the figure 7.b). The ^{36}Cl concentrations of the data and of the best model are represented together with the estimated inheritance. These chronological data points toward a cluster of ages corresponding to the Early Holocene (9-12 ka), and another to the Late Glacial Maximum (LGM) at ~20 ka.

mm/yr, which is in the range of possible erosion rates in similar environments (~20-60 mm/ka; e.g., Ryb et al. (2014), Sadier et al. (2012) and Thomas et al., (2018). Thus, assuming a mean denudation rate of 30 mm/kyr, this sample can only provide a minimum age of 195.57 ± 45.30 ka. However, the other two samples are likely not saturated as their maximum denudation rate is relatively high (77 mm/yr and 83 mm/kyr). From these two samples we derive an age of 53.47 ± 11.64 ka and 49.80 ± 10.78 ka assuming that no erosion affected the surface. Considering the longer exposure duration, we also calculated the CRE ages for a mean denudation rate of 30 mm/kyr, which led to 78.55 ± 17.10 ka and 71.34 ± 15.44 ka. Three charcoals collected above the sampled pebbles within the 1.60 m thick clayey unit were also analyzed (Table 2) and led to ages of 303-462 yr BP, 921-1049 yr BP and 23441-24087 yr BP. In addition, we also dug a second pit (pit 2, Figure 11a) in the remnant surface ~10 m above the terrace holding pit 1. The same clayey unit was found over at least 1.5 m and two charcoals were collected from it, giving ages of 4530-4746 yr BP and 10153-10889 yr BP (Table 2).

The alluvial deposits found at the top of the quarry along the eastern branch of the paleo-Kupa canyon were also sampled for cosmogenic dating (site pK, Figure 3b and Figure4b). Three samples collected between 4.8

m and 5.5 m depth from the surface were analyzed, but all revealed low maximum denudation rates, from 34.6 mm/kyr to 39 mm/kyr. which likely indicate that the steady state equilibrium was reached. The derived minimum exposure time from these pebbles was then calculated for a denudation rate of 30 mm/yr and gave CRE minimum ages ranging from 227.41 ± 62.76 ka to 303.56 ± 83.28 ka (Table 1).

6 Discussion

6.1 Late-Quaternary Chronological Constraints

Geomorphic markers, such as fan and alluvial terraces or colluvium deposits, and their relationship with regional Quaternary climatic conditions have not been studied with modern dating approaches in Central Croatia, to date. Only loess deposits have been dated recently at Bilogora (NE of Zagreb), using the post-IR IRSL technique, leading to terrace formation along the Drava River at >359 ka and >450 ka (*Wacha et al.*, 2018). The main objective of our dating work is first to constrain the age of geomorphic landforms displaced by the PPKF, but it will also provide chronological benchmarks for further geomorphological work in Central Croatia.

The radiocarbon ages measured in this study (Table 2) show a wide dispersion and must be handled with care. At Cepeliš site S1, the two radiocarbon ages from the alluvial terrace are very young, <507-618 yr BP, and likely corresponds to human activities or roots burnt during wildfires as the two samples were collected in the near-surface (~30 cm). Historical ages are also found in the clayey layer of pit 1 at Cepeliš site S3, from 303 yr BP to 1049 yr BP, and might also be related to post-deposit burned roots. However, older ages are also found in the upper clayey deposits of pit 1 (25391-26037 BP) and pit 2 (6480-6696 and 12103-12839 BP), which suggest that the emplacement of the clayey unit is related to late Quaternary events. The context of deposition of these clays is unclear, they could originate from slope deposits of clay units eroded from the hillside, or from the Upper Miocene and Plio-Quaternary lacustrine series of the Pannonian Basin. Additional constraints come from the underlying conglomerate in pit 1 (Figure 12b) that gives ^{36}Cl CRE ages compatible with the 4th Marine Isotopic Stage (MIS 4), with at least ~50 ka if we consider that no erosion affected the surface since its deposition, and ~70 ka if we assume a denudation rate of 30 mm/kyr (Table 1). We can then assume that even if the number of radiocarbon samples is small and the ages are scattered, the radiocarbon data could be explained by Late Quaternary processes, with modelling of the current relief either during MIS 4 (CRE ages around 50-70 ka), the LGM period (radiocarbon age of 25.4-26.0 ka BP in the terrace of pit 1), and later during the Early and Middle Holocene at the base of the hill where pit 2 was opened (ages of 6.5-6.7 and 12.1-12.8 ka BP).

At the sites Cepeliš S1and S2, located on the CMUS and CMLS of the CSPF, we found two cosmogenic age clusters of 3.8 ± 1.3 ka and 10.3 + 2.7/−3.1 ka (without erosion, Figure 15a) for the samples collected within the alluvial terraces (Figures 6a and 7a), and one older age at 19.8 ± 2.49 ka. Two possible scenarios arise from this age dispersion. On the one hand, the inheritance of some boulders could explain the older ages, while on the other hand, the deposition of more recent boulders from the hillslopes could explain the younger ones. Another constraint is coming from the colluvium dated at the Cepeliš site S1 from which the ^{36}Cl depth profile reveals an exposure time of 11.65 ± 1.21 ka (Table 1 and Figure 14b). According to previous studies around Europe (*Tebbens et al.*, 1999; *Mol et al.*, 2000) and the Mediterranean Sea (*Moulin et al.*, 2014, 2016; *Pousse-Beltran et al.*, 2022; *Gemignani et al.*, 2022) a post-LGM incision phase is expected, in particular after the Younger Dryas ~12 kyr ago. Based on these data, an initial interpretation of the ages would be to consider that both the incision and abandonment of alluvial terraces and the deposition of colluvium occurred in the Hrastovica hills after ~12 ka, which is consistent with the age cluster of 10.3 + 2.7/−3.1 ka and the age of 11.29 ± 1.19 ka derived from the depth profile. However, the older age of 19.8 ± 2.49 ka also suggest that the area was affected during the LGM period, which is also expected as studies in the northern Dinarides revealed marker ages at 23.5 ± 5.5 ka (*Moulin et al.*, 2016) and a set of alluvial terraces along major rivers in Albania shows abandonment at 27-24 ka and 22-16.5 ka (*Guzmán et al.*, 2024; *Mugnier et al.*, 2024).

In order to integrate these dating results into a more global understanding of the processes that have affected the region, we can interpret the distribution of the ages in view of the climatic events that have affected Europe since the last glacial cycle. Our data suggest three possible, and potentially non-exclusive, scenarios concerning the ages of Late Quaternary climatically driven events that influenced the evolution of the drainage network, with incision phases either during the MIS 4 (~50-75 ka), the LGM (~17-26 ka) and the early Holocene (~7-13 ka). On one hand, we have ages that support terrace abandonment or slope wash materials at 10.3 + 2.7/−3.1 ka if we take the sum of the probability density functions from the sites S1 and S2 at Cepeliš (Figure 15a). On the other hand, we can assume an incision phase during the LGM ([17.3 - 26] ka) supported by the radiocarbon age of the pit 1 from the sites S3 at Cepeliš ([25.4 - 26.0] ka BP) and the one from the cosmogenic sample in the terrace from site S1 at Cepeliš (19.8 ± 2.5 ka). Finally, the hypothesis of MIS 4 ages cannot be ruled out, as two samples from site S1 at Cepeliš yielded ages exceeding 50–70 ka.

Lastly, the CRE ages from the quarry along the paleo-Kupa canyon only provide a minimum age of about ~300 ka, assuming a denudation rate of 30 mm/kyr.

To sum up, despite the scattered ages, the results suggest that Late Quaternary processes drove river incision and terrace abandonment. Although robust constraints on alluvial terrace sequences are lacking in the area, several studies from the peri-Adriatic region, such as in Slovenia (Pavich and Vidic, 1993 ;

Vidic and Lobnik, 1997) and Albania (Guzmán et al., 2023; Mugnier et al., 2024), have shown that these three periods were associated with terrace formation. Therefore, the study area was likely affected by each of these climatic events.

6.2 Late-Quaternary Fault Slip Rates

At the three studied sites, the measured offsets are on the order of 4 m to 24.1 m and the chronological analysis revealed potential ages of terraces abandonment from the MIS 4 (~50-75 ka) to the early Holocene (i.e., after ~12 ka). In the following, to estimate fault slip rates we will mostly consider offset measurements derived from the lowest terraces (results compiled in Figure S6 in the Supporting Information) and ages corresponding to three plausible terrace abandonment ages: 1) the MIS 4 (50-75 ka), 2) the LGM period (17.3-26 ka), or 3) the early Holocene with locally constrained values of 10.3 +2.7/−3.1 ka (Figure 15a).

The CMUS at Cepeliš is constrained by two sites, S1 and S2a. At Cepeliš site S1, the preferred estimated offsets range between 15.5 to 22.6 m with a mean value of 17.9 m (Figure 6b), and at Cepeliš site S2a the preferred estimates are of 4 to 7.3 m with a mean value of 5.7 m (Figure 8b). Combining these offsets with the "MIS 4", "LGM" or "early Holocene" hypotheses, we find that the CMUS has a slip rate of 0.3 to 0.5 mm/yr at Cepeliš site S1 and ~0.1 mm/yr at site S2a to the north considering the MIS 4 hypothesis, 0.7 to 1.0 mm/yr at site S1 and 0.2 to 0.3 mm/yr at site S2a considering the LGM hypothesis, and 1.4 to 2.5 mm/yr at site S1 and 0.5 to 0.8 mm/yr at site S2a assuming an early Holocene hypothesis (Figure 16a and Figure S6). Interestingly, the slip rate estimates are lower at site S2 to the NW, potentially because it corresponds to the NW end of the CMUS segment and that the cumulative slip here is mostly absorbed by the CMLS strand downhill.

On the lower strands at Cepeliš are constrained by the site S2b (CMLS) and S3 (CSLS). The measured offsets at site S2b gives a range of preferred offsets of 10.5 to 24.1 m with a mean value of 17.3 m (Figure 9b), and the preferred offset from the site S3 range from 8 to 11.5 m with a mean value of 9.8 m (Figure 11b). Combining these offsets with the "MIS 4", "LGM" or "early Holocene" hypotheses, we find that the CMLS has a slip rate of 0.1 to 0.5 mm/yr at Cepeliš site S2b and that the CSLS slip rate at site S3 is 0.1 to 0.2 mm/yr considering the MIS 4 hypothesis, 0.7 to 1.0 mm/yr at site S2b and 0.4 to 0.6 mm/yr at site S3 considering the LGM hypothesis, and 1.4 to 2.4 mm/yr at site S2b and 0.8 to 1.4 mm/yr at site S3 assuming an early Holocene hypothesis (Figure 16a and Figure S6). Compared to the sites along the upper strand (CMUS), the trend is here reversed has the lower strand CMLS seems to slip at faster rates than the CSLS to the SE. Knowing that the CSLS and CMLS merge midway between the two sites (S2b and S3), the question arises whether this along-strike slip inversion between the upper and lower strands is due to the fact that we are missing deformation on the CMLS at site S1, although no offsets are detected here (absent or unquantifiable), or whether a similar budget of slip is absorbed along the entire CSPF, in which case it could be a transfer of the strain from the upper to the lower strands towards the NW.

Toward the southeast, the preferred offset at the Gornja Budičina site on the DBSPF range from 17.3 to 21.5 m (Figure 14b), with a mean offset of 19.4 m. Although we didn't succeed to date the alluvial surface downstream of the fault in this area, the limited incision and the similarity of this terrace with those encountered and dated at Cepeliš, we propose slip rate estimates based on the MIS 4, LGM and early Holocene hypotheses. Considering MIS 4 ages, we can infer slip rates of 0.2 to 0.4 mm/yr, while assuming LGM or early Holocene ages we estimate potential slip rates of 0.7 to 1.1 mm/yr and 1.6 to 2.7 mm/yr respectively (Figure 16a and Figure S6).

Based on these estimations, a total slip rate along the CSPF at Cepeliš can be approached if we combine slip rates from the upper and lower strands. The simplest case is to combine the estimates of slip rates on the CMUS and CMLS at sites S2a and S2b, which results in a total slip rate of 0.2 to 0.6 mm/yr with the MIS 4 hypothesis, 0.9 to 1.3 mm/yr considering LGM ages, and of 1.8 to 3.2 mm/yr with the early Holocene age constraints. Although the deformation might be spread over more strands to the SE, we can also estimate a total slip rate based on the values derived at Cepeliš site S1 (CMUS) and S3 (CSLS), which results in a total slip rate of 0.4 to 0.7 mm/yr with the MIS 4 hypothesis, 1.1 to 1.6 mm/yr considering LGM ages, and 2.2 to 3.9 mm/yr using early Holocene age constraints. These total slip rates are based on strong assumptions and the range of uncertainties is wide, but it's worth noting that they are of the same order, and compatible with the slip rate derived further south at Gornja Budičina (~0.2 to 0.4 mm/yr, ~0.7 to 1.1 mm/yr and ~1.6 to 2.7 mm/yr for the MIS 4, LGM and early Holocene hypotheses respectively).

According to the European active fault database of *Basili et al.* (2013, 2024), the estimated slip rate for the PPKF from indirect geological and geodynamics inferences ranges from 0.08 mm/yr to 0.2 mm/yr. Our work demonstrates that such values must be revised upwards to at least 0.2 mm/yr, and that the fault geometry of the Petrinja fault is not compatible with a NE-verging thrust fault. Nevertheless, given the current tectonic context, we agree that the upper bounds of the slip rates estimated here are very high and unlikely, that is why we favor the MIS 4 and LGM hypotheses in our conclusions. Considering the MIS 4 at the origin of the youngest offset markers, this study estimates a loading rate of the Petrinja fault of the order of 0.2 to 0.7 mm/yr over the last ~50-75 kyr, and potentially around 1 mm/yr considering younger LGM ages. However, the slip rates inferred from the early Holocene hypothesis largely exceed the detectable geodetic rates (approximatively 1 mm/yr based on GNSS time series), and such values are not plausible unless the loading rate has decreased during the past 10 kyr.

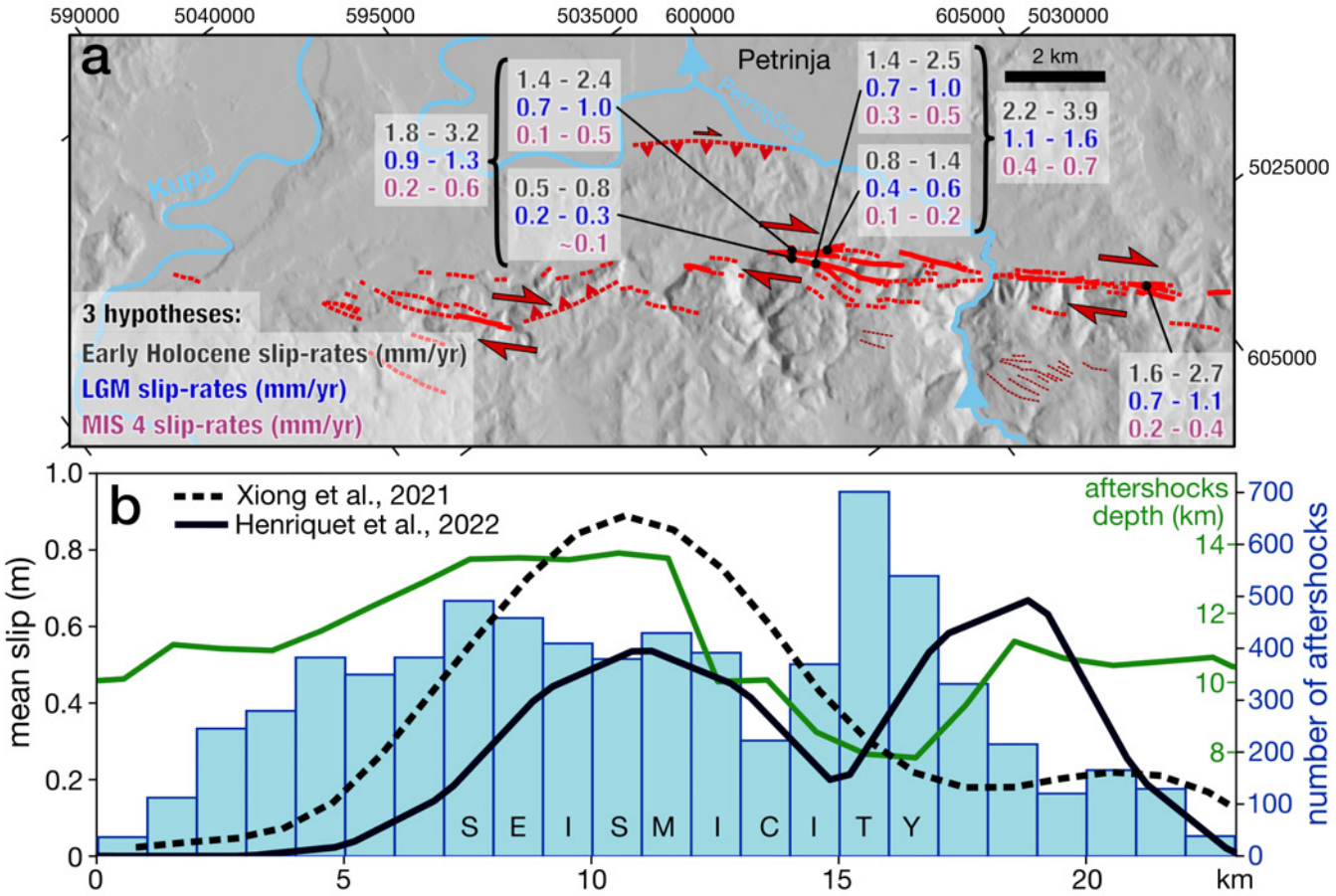

Figure 16 – Along-strike segmentation of the long-term Petrinja Fault compared with the 2020 earthquake source. a) Morphotectonic map of the Petrinja Fault with the estimated fault-slip rates from this study. The derived fault-slip rates come from the analysis of geomorphological markers and three hypotheses concerning their potential ages: markers formed during the MIS 4 event at ~50-75 ka, the Late Glacial Maximum at ~17-24 ka or during the Early Holocene at ~7-13 ka. b) Along-strike strike-slip slip averaged over the fault depth for the 2020 Petrinja earthquake and aftershocks distribution from *Herak and Herak* (2023). The black dashed line corresponds to the InSAR-based slip model of *Xiong et al.* (2022) and the continuous black line to the benchmark-based slip inversion from *Henriquet et al.* (2022), showing respectively a single patch slip model and a more complex solution with two slip patches. The median depth of the aftershocks along-strike, represented with the green line, highlights with the distribution of aftershocks a spatial clustering that follows at first order the fault segmentation at the surface.

6.3 Comparison with the 2020 Coseismic Rupture and Seismic Hazard along the PPKF

Consistently with the mapped long-term fault trace, the surface ruptures observed after the 2020 Petrinja earthquake were discontinuous and characterized by multi-kilometer en échelon left-stepping or parallel sections forming a wide deformation zone (*Baize et al.*, 2022). Interestingly, the maximum right-lateral coseismic offsets were measured at about 30-40 cm (*Baize et al.*, 2022), while geodetic benchmarks revealed a mid-field total displacement at the surface of >1.2 m (*Henriquet et al.*, 2022) and the geodetic-based slip inversions pointed toward a maximum slip at shallow depth of ~2-3 m (*Xiong et al.*, 2022; *Ganas et al.*, 2021; *Henriquet et al.*, 2022; *Zhu et al.*, 2023). This suggests that, although the main slip occurred at a shallow depth, <7 km, the released strain did not fully propagate and localize on a single strand at the surface (Figure 16). The decrease of slip towards the surface (<3 km), namely the slip deficit, is a long-lived debated issue (e.g., *Barbot et al.*, 2008; *Xu et al.*, 2016; *Milliner et al.*, 2020; *Marchandon et al.*, 2021). This shallow slip deficit implies that the strain either distributes or diffuses within a volume at the surface during the rupture process (*Fialko et al.*, 2005; *Antoine et al.*, 2021, 2022), or that the lacking slip is recovered by postseismic or interseismic aseismic creep (*Marone et al.*, 1991; *Wei et al.*, 2009; *Cakir et al.*, 2023), or that other superficial coseismic events count in the strain budget such as the Mw 4.9 2019 Teil earthquake in France (rupture depth <1 km, *Marconato et al.*, 2023). Previous works also showed that shallow slip deficit is related to immature fault systems (*Dolan and Haravitch*, 2014; *Pousse-Beltran et al.*, 2020; *Li et al.*, 2020). Although it is difficult to state what case affects the Petrinja fault, the large coseismic slip, small rupture size and high stress drop of the 2020 earthquake (*Žilić et al.*, 2025) is consistent with a geometrically complex and relatively immature fault system in the present-day regional kinematics (*Ross et al.*, 2018; *Xiong et al.*, 2022; *Žilić et al.*, 2025). Such assumption has implications on the determination of fault slip rates and hazard assessment, which are most often based on

discrete surface offsets. Therefore, the complexity of the fault system and the 2020 rupture together with the apparent surface slip deficit suggest that the PPKF is likely an immature fault and that the localization of the surface deformation may not fully represent the total strain budget, and thus the estimated slip rate should be considered as minimum values. On the other hand, it should be remembered that most of the fault trace is located on vegetated lands, part of which is not accessible because of remaining minefields in the area (*Baize et al.*, 2022), and thus the mapping of brittle coseismic deformation is likely incomplete.

The slip-rate estimation in this study can also be compared to the slip budget from the 2020 Petrinja earthquake in order to frame the recurrence time of magnitude >6 earthquakes on the Petrinja fault. Let's assume that the PPKF can produce characteristic earthquakes similar to the magnitude 6.4 Petrinja earthquake, with surface displacements at geomorphological scale in the range of 20 cm to 50 cm. Such a range of displacements fall in between the surface ruptures measured on the field (Baize et al., 2022) and the subsurface displacements constrained by geodetic-based slip inversions (*Xiong et al.*, 2022; *Henriquet et al.*, 2022), and thus takes into account the inferred distribution of subsurface deformation as discussed above. Now, using the potential slip-rates derived here from this study, in the order of 0.7 mm/yr to 1 mm/yr (taking lower bound estimates), we found recurrence times of 200 years to ~700 years.

The 2020 Petrinja earthquake also revealed from the main shock focal mechanism and the distribution of aftershocks (*Baize et al.*, 2022; *Herak and Herak*, 2023) and the geodetic-based slip inversions (*Xiong et al.*, 2022; *Ganas et al.*, 2021; *Henriquet et al.*, 2022; *Zhu et al.*, 2023) that the main fault dips 70-90° SW-ward, consistently with the transpressive regime and the building of the Hrastovica hills. Although the vertical deformation related to the 2020 earthquake is rather small if not negligible (*Henriquet et al.*, 2022), potential coseismic uplift of the northwestern sector around the paleo-Kupa area is predicted by InSAR measurements (*Zhu et al.*, 2023). Furthermore, the slip inversions based on the civilian benchmark measurements from *Henriquet et al.* (2022) also confirmed that the deformation distributes over multiple fault strands. Indeed, the main evidence for a long-term fault strand along the hill SW from Petrinja mostly comes from the significant relief (~100 m) and the seismic section from Figure 2b, but the slip solutions for the 2020 earthquake also predict slip on this secondary structure (Figure 16).

We also note that the 2020 earthquake mainly ruptured the central and northern part of the PPKF where clear traces of the long-term fault are scarce (Figure 16). Interestingly, the deeper slip patch predicted by the inversion of civilian benchmark measurements (Henriquet et al., 2022) extends to the SE below the Donja Budičina section, while the surface expression of the Petrinja Fault is quite clear in this area, suggesting a localized deformation at the surface over multiple seismic cycles (Figure 16). As shown by Coulomb failure stress changes (*Herak and Herak*, 2023; *Zhu et al.*, 2023), the expected increase in stress towards the SE should facilitate future earthquakes in the southeastern continuation of the PPKF.

6.4 Fault Growth and Fault Maturity

The morphotectonic fault trace shows multiple sub-parallel and en echelon segments of the Petrinja Fault consistent with the flower structure geometry from *Baize et al.* (2022). The continuation of the PPKF northward on the Pokupsko section remains, however unknown along the Vukomeričke gorice hills, the epicentral area of the 1909 Kupa Valley earthquake. According to the focal mechanism analysis of the 1909 earthquake derived from low quality and sparse measurements at that time (*Herak and Herak*, 2010), the ruptured fault corresponds to a SW verging thrust whose inferred surface trace makes at a larger scale a left-stepping segment from the 2020 rupture trace. In such a case we can expect that the system is mostly transpressive, with a restraining bend configuration at the origin of the Hrastovica topography growth. However, the longitudinal valley along the Vukomeričke gorice hills ridge might also represent a significant fault segment, and in that case, the broad-scale geometry of the PPKF would show a left-stepping segmentation that would produce a releasing bend in the Novi Farkašić area (Figures 3 and 4). According to post-seismic InSAR measurements (*Baize et al.*, 2022), the 2020 post-seismic slip propagated toward this along-ridge segment, supporting the releasing bend configuration. Then, if the current knowledge on active deformation cannot really discriminate which structure prevails in the NW-continuation of the Petrinja Fault, additional constraints come from the long-term geological and geomorphological data. Indeed, as outlined by the seismic section, Neogene and pre-Neogene units are exhumed along the Petrinja Fault and the drainage network records knickpoints and the abandonment of the "paleo-Kupa" gorge along the northern Hrastovica hills, all evidencing a recent or current uplift activity. The alluvial sediments inferred from the paleo-Kupa river before its incision and later abandonment unfortunately only give a minimum age of exposure of about 300 ka. This still allows us to estimate a maximum mean uplift rate for this zone of about ~0.3 mm/yr considering that the karstic plateau where the paleo-Kupa incised (~230 m a.s.l.) is ~100 m above the downstream plain shaped by the paleo-Kupa east of Gornje Mokrice (~130 m a.s.l.).

The long-term offset described in this study covers a relatively small range of offset markers (<23 m) of Holocene to LGM ages. As the fault has certainly been active over a much longer period, larger offset landforms could potentially be observed along the PPKF. *Baize et al.* (2022) proposed on the Cepeliš site a back-slipping on the lower branch of about 315 m and on the upper branch of about 260 m by using the stream and valley axis as piercing lines. Such displacements must be handled with care as the morphotectonic interpretation

is uncertain, but assuming roughly a mean cumulative slip rate of about ~0.2 to 1 mm/yr, that would mean that the drainage network was in place 0.5 to 3 Myr ago, i.e., during the Pleistocene.

7 Conclusion

Using field observations and high-resolution DEMs, we mapped the portion of the Petrinja Fault that ruptured in 2020 and southward over 20 km. The fault geometry appears relatively discontinuous and is characterized by a main fault strand striking 130-140°N, about 10-km-long from Donja Budičina to Cepeliš and 1-4-km-long left-stepping segments toward the NW. The 2020 rupture is consistent with the mapped fault trace, which suggests that the deformation is repeatedly accommodated at the surface by a series of small fault sections. Right-lateral cumulative offsets from 4 to 24.1 m (locally up to 107 m) were measured along the main fault strands and dating results indicate ages of offset markers from the MIS 4 (~50-75 ka), the LGM (~17 to 26 ka) or the Early Holocene period (~7 to 13 ka). Based on these results, we provide the first direct estimation of fault slip rates on the central and southern portions of the Petrinja Fault section in the central part of the PPKF. Assuming a common MIS 4 or LGM age of the investigated landforms, the estimated fault slip rates are 0.2 to 0.7 mm/yr and 0.7 to 1.6 mm/yr respectively. In contrast, considering Early Holocene ages would imply unlikely high slip rates of 1.6 to 3.9 mm/yr, which are inconsistent with the current tectonic setting. Although the Petrinja fault lies within a low strain intraplate region, this work demonstrates that a detailed morphotectonic analysis can provide valuable constraints for seismic hazard assessment. Our conclusion indicates that the minimum fault slip rate that should be taken into account for the Petrinja fault is 0.2 mm/yr, a value significantly higher than that inferred in the European seismic source database.

Acknowledgements

The Lidar data was acquired in 2021 by Flycom Aviation Company and co-funded by the Croatian, Italian, Slovenian and French institutions. CNES is warmly acknowledged for providing us with the Pléaides satellite images through ISIS and CEOS_seismic pilot (ESA) programs. We would also like to thank the Croatian State Geodetic Administration for providing orthophotos in the Petrinja area. We are thankful to SARM-CRPG (France) for performing the chemical measurements. The ASTER French AMS national facility (CEREGE, Aix-en-Provence) is supported by the INSU/CNRS, the French Ministry of Research and Higher Education, IRD, and CEA. This work has been conducted in the frame of a consortium of researchers that have received fundings from the programme TelluS of the Institut National des Sciences de l'Univers, CNRS, and from the CNES in the frame of the CRYZ and BALKASAR projects. M. Henriquet benefits from a CNES postdoctoral fellowship. The french-croatian collaboration has been supported by a PHC project in the frame of the COGITO Campus France program. This research was also conducted in the scope of the internal research project GeoSAVAGE at the Croatian Geological Survey, funded by the National Recovery and Resilience Plan 2021–2026 of the European Union – NextGenerationEU, and monitored by the Ministry of Science and Education of the Republic of Croatia (BK, JM, NB, MŠ, MB). PJR acknowledges the support of the Slovenian Research and Innovation Agency (ARIS) through the program group Dynamic Earth (P1-0419) and RSF-O ACTIVIST2CRO project. The authors would like to thank Régis Braucher for the fruitful discussion on cosmogenic datings. We acknowledge also the financial support of the Italian Embassy of Zagreb (project "Earthquake Geology studies in Central Croatia" and of the Section Rome1 of the Istituto Nazionale di Geofisica e Vulcanologia.

Author contributions

M.H. realized the analysis, collected samples during field campaigns and wrote the paper. **L.B., S.B., B.K., J.M., N.B., M.S., M.B., D.P., F.C., S.P., A.T., P.B., B.P., P.J.R., A.M., R.C.** participated in field campaigns and helped to the the analysis and revision of the manuscript. **M.M.** made corrections to the article. **L.B.** and **M.M.** provided the necessary funding to carry out this work.

Data availability

The large-scale FABDEM was downloaded from the University of Bristol via (https://research-information.bris.ac.uk/en/datasets/fabdem-2/) and the LiDAR DTM is available at a resolution of 0.5 m in the EaSy Data repository at the following link: https://www.easydata.earth/#/public/metadata/3f9c129f-b1c4-4780-9fd1-74f0cce568ec (with the DOI: https://doi.org/10.57932/3f9c129f-b1c4-4780-9fd1-74f0cce568ec).

Competing interests

The authors declare no competing interests.

Peer review

This publication was peer-reviewed by Alex Hatem and an anonymous reviewer. The full peer-review report can be found here: Review Report.

Copyright notice

References

Antoine, S. L., Y. Klinger, A. Delorme, K. Wang, R. Bürgmann, and R. D. Gold (2021), Diffuse deformation and surface faulting distribution from submetric image correlation along the 2019 Ridgecrest, California, ruptures, *Bulletin of the Seismological Society of America*, *111*(5), 2275–2302, https://doi.org/10.1785/0120210036.

Antoine, S. L., Y. Klinger, A. Delorme, and R. D. Gold (2022), Off-fault deformation in regions of complex fault geometries: The 2013, M_w 7.7, Baluchistan rupture (Pakistan), *Journal of Geophysical Research. Solid Earth*, *127*(11), e2022JB024,480, https://doi.org/10.1029/2022jb024480.

Arnold, M., S. Merchel, D. L. Bourlès, R. Braucher, L. Benedetti, R. C. Finkel, G. Aumaître, A. Gottdang, and M. Klein (2010), The French accelerator mass spectrometry facility ASTER: Improved performance and developments, *Nuclear Instruments & Methods in Physics Research. Section B, Beam Interactions With Materials and Atoms*, *268*(11-12), 1954–1959, https://doi.org/10.1016/j.nimb.2010.02.107.

Atanackov, J., P. Jamšek Rupnik, J. Jež, B. Celarc, M. Novak, B. Milanič, A. Markelj, M. Bavec, and V. Kastelic (2021), Database of active faults in Slovenia: Compiling a new active fault database at the junction between the Alps, the Dinarides and the Pannonian Basin tectonic domains, *Frontiers in Earth Science*, *9*, 604,388, https://doi.org/10.3389/feart.2021.604388.

Bada, G., G. Grenerczy, L. Tóth, F. Horváth, S. Stein, S. Cloetingh, G. Windhoffer, L. Fodor, N. Pinter, and I. Fejes (2007), Motion of Adria and ongoing inversion of the Pannonian Basin: Seismicity, GPS velocities, and stress transfer, in *Continental Intraplate Earthquakes: Science, Hazard, and Policy Issues*, pp. 243–262, Geological Society of America, https://doi.org/10.1130/2007.2425(16).

Baize, S., S. Amoroso, N. Belić, L. Benedetti, P. Boncio, M. Budić, F. R. Cinti, M. Henriquet, P. Jamšek Rupnik, B. Kordić, S. Markušić, L. Minarelli, D. Pantosti, S. Pucci, M. Špelić, A. Testa, S. Valkaniotis, M. Vukovski, J. Atanackov, J. Barbača, M. Bavec, R. Brajkovič, V. Brčić, M. Caciagli, B. Celarc, R. Civico, P. M. De Martini, R. Filjak, F. Iezzi, A. Moulin, T. Kurečić, M. Métois, R. Nappi, A. Novak, M. Novak, B. Pace, D. Palenik, and T. Ricci (2022), Environmental effects and seismogenic source characterization of the December 2020 earthquake sequence near Petrinja, Croatia, *Geophysical Journal International*, *230*(2), 1394–1418, https://doi.org/10.1093/gji/ggac123.

Balling, P., B. Tomljenović, S. M. Schmid, and K. Ustaszewski (2021), Contrasting along-strike deformation styles in the central external Dinarides assessed by balanced cross-sections: Implications for the tectonic evolution of its Paleogene flexural foreland basin system, *Global and Planetary Change*, *205*(103587), 103,587, https://doi.org/10.1016/j.gloplacha.2021.103587.

Balázs, A., L. Matenco, I. Magyar, F. Horváth, and S. Cloetingh (2016), The link between tectonics and sedimentation in back-arc basins: New genetic constraints from the analysis of the Pannonian Basin: SEISMIC ANALYSIS OF THE PANNONIAN BASIN, *Tectonics*, *35*(6), 1526–1559, https://doi.org/10.1002/2015tc004109.

Barbot, S., Y. Fialko, and D. Sandwell (2008), Effect of a compliant fault zone on the inferred earthquake slip distribution, *Journal of Geophysical Research*, *113*(B6), https://doi.org/10.1029/2007jb005256.

Basili, R., V. Kastelic, M. B. Demircioglu Tumsa, D. Garcia Moreno, E. S. Nemser, P. Petricca, S. P. Sboras, G. M. Besana-Ostman, J. Cabral, and T. Camelbeeck (2013), European database of seismogenic faults (EDSF), *European Database of Seismogenic Faults (EDSF)*.

Basili, R., L. Danciu, C. Beauval, K. Sesetyan, S. P. Vilanova, S. Adamia, P. Arroucau, J. Atanackov, S. Baize, C. Canora, R. Caputo, M. M. C. Carafa, E. M. Cushing, S. Custódio, M. B. Demircioglu Tumsa, J. C. Duarte, A. Ganas, J. García-Mayordomo, L. Gómez de la Peña, E. Gràcia, P. Jamšek Rupnik, H. Jomard, V. Kastelic, F. E. Maesano, R. Martín-Banda, S. Martínez-Loriente, M. Neres, H. Perea, B. Šket Motnikar, M. M. Tiberti, N. Tsereteli, V. Tsironi, R. Vallone, K. Vanneste, P. Zupančič, and D. Giardini (2024), The European Fault-Source Model 2020 (EFSM20): geologic input data for the European Seismic Hazard Model 2020, *Natural Hazards and Earth System Sciences*, *24*(11), 3945–3976, https://doi.org/10.5194/nhess-24-3945-2024.

Bočić, N. (2021), Structural-geomorphological aspects of the Petrinja earthquake M6. 2 (Croatia)-preliminary considerations, *Croatian Geographical Bulletin*, *83*(1), 5–24.

Braucher, R., P. Del Castillo, L. Siame, A. J. Hidy, and D. L. Bourlés (2009), Determination of both exposure time and denudation rate from an in situ-produced 10Be depth profile: A mathematical proof of uniqueness. Model sensitivity and applications to natural cases, *Quaternary Geochronology*, *4*(1), 56–67, https://doi.org/10.1016/j.quageo.2008.06.001.

Brčić, V., I. Dunkl, A. Mindszenty, M. Brlek, N. Trinajstić, P. Bajo, B. Bauluz, I. Mišur, V. Karius, S. Šuica, D. Kukoč, A. Yuste, E. Laita, H. Von Eynatten, and A. Zeh (2023), A time-space window between Eocene karst bauxite genesis and the first molasse deposition in the Dinaric Foreland Basin in the North Dalmatia, Croatia, *Frontiers in Earth Science*, *11*(1224164), 1224,164, https://doi.org/10.3389/feart.2023.1224164.

Cakir, Z., U. Doğan, A. M. Akoğlu, S. Ergintav, S. Özarpacı, A. Özdemir, T. Nozadkhalil, N. Çakir, C. Zabcı, M. H. Erkoç, M. Basmenji, M. Köküm, and R. Bilham (2023), Arrest of the Mw 6.8 January 24, 2020 Elaziğ (Turkey) earthquake by shallow fault creep, *Earth and Planetary Science Letters*, *608*(118085), 118,085, https://doi.org/10.1016/j.epsl.2023.118085.

Dolan, J. F., and B. D. Haravitch (2014), How well do surface slip measurements track slip at depth in large strike-slip earthquakes? The importance of fault structural maturity in controlling on-fault slip versus off-fault surface deformation, *Earth and Planetary Science Letters*, *388*, 38–47, https://doi.org/10.1016/j.epsl.2013.11.043.

Ferrater, M., R. Arrowsmith, and E. Masana (2015), Lateral offset quality rating along low slip rate faults: Application to the Alhama de Murcia fault (SE Iberian Peninsula), *Remote Sensing*, *7*(11), 14,827–14,852, https://doi.org/10

.3390/rs71114827.

Fialko, Y., D. Sandwell, M. Simons, and P. Rosen (2005), Three-dimensional deformation caused by the Bam, Iran, earthquake and the origin of shallow slip deficit, *Nature*, *435*(7040), 295–299, https://doi.org/10.1038/nature03425.

Ganas, A., National Observatory of Athens, P. Elias, S. Valkaniotis, V. Tsironi, I. Karasante, P. Briole, National Observatory of Athens, National Observatory of Athens, National Observatory of Athens, and École Normale Supérieure de Paris (2021), Petrinja earthquake moved crust 10 feet, *Temblor*, https://doi.org/10.32858/temblor.156.

Gemignani, L., B. V. Mittelbach, D. Simon, A. Rohrmann, M. U. Grund, A. Bernhardt, K. Hippe, J. Giese, and M. R. Handy (2022), Response of drainage pattern and basin evolution to tectonic and climatic changes along the dinarides-Hellenides orogen, *Frontiers in Earth Science*, *10*, 821,707, https://doi.org/10.3389/feart.2022.821707.

Gosse, J. C., and F. M. Phillips (2001), Terrestrial in situ cosmogenic nuclides: theory and application, *Quaternary Science Reviews*, *20*(14), 1475–1560, https://doi.org/10.1016/s0277-3791(00)00171-2.

Gromig, R., S. Mechernich, A. Ribolini, B. Wagner, G. Zanchetta, I. Isola, M. Bini, and T. J. Dunai (2018), Evidence for a Younger Dryas deglaciation in the Galicica Mountains (FYROM) from cosmogenic 36Cl, *Quaternary International: The Journal of the International Union for Quaternary Research*, *464*, 352–363, https://doi.org/10.1016/j.quaint.2017.07.013.

Grünthal, G., R. Wahlström, and D. Stromeyer (2013), The SHARE European Earthquake Catalogue (SHEEC) for the time period 1900–2006 and its comparison to the European-Mediterranean Earthquake Catalogue (EMEC), *Journal of Seismology*, *17*(4), 1339–1344, https://doi.org/10.1007/s10950-013-9379-y.

Guzmán, O., J.-L. Mugnier, R. Vassallo, R. Koçi, J. Carcaillet, and F. Jouanne (2024), Fluvial terrace formation in mountainous areas: (1) Influence of climate changes during the last glacial cycle in Albania, *Comptes rendus: Geoscience*, *355*(G2), 331–353, https://doi.org/10.5802/crgeos.251.

Hawker, L., P. Uhe, L. Paulo, J. Sosa, J. Savage, C. Sampson, and J. Neal (2022), A 30m global map of elevation with forests and buildings removed, *Environmental research letters*, *17*(2), 024,016, https://doi.org/10.1088/1748-9326/ac4d4f.

Henriquet, M., A. Moulin, M. Vukovski, B. Kordić, M. Budić, J. Hollingsworth, R. Gold, S. Baize, and L. Benedetti (2021), Comparison between the coseismic surface displacement during the 29 December 2020 Mw 6.4 Petrinja earthquake (Croatia) from optical image correlation and long-term geomorphological observations of cumulative displacements, in *EGU General Assembly 2021*, pp. EGU21–16,590, Copernicus GmbH, Vienna, Austria, https://doi.org/10.5194/egusphere-egu21-16590.

Henriquet, M., B. Kordic, M. Métois, C. Lasserre, S. Baize, L. Benedetti, M. Spelić, and M. Vukovski (2022), Rapid remeasure of dense civilian networks as a game-changer tool for surface deformation monitoring: The case study of the M_w 6.4 2020 Petrinja earthquake, Croatia, *Geophysical Research Letters*, *49*(24), e2022GL100,166, https://doi.org/10.1029/2022gl100166.

Herak, D., and M. Herak (2010), The kupa valley (Croatia) earthquake of 8 October 1909–100 years later, *Seismological Research Letters*, *81*(1), 30–36, https://doi.org/10.1785/gssrl.81.1.30.

Herak, D., M. Herak, and B. Tomljenović (2009), Seismicity and earthquake focal mechanisms in North-Western Croatia, *Tectonophysics*, *465*(1-4), 212–220, https://doi.org/10.1016/j.tecto.2008.12.005.

Herak, M. (2025), Croatian catalogue and database of focal mechanism solutions, characteristic mechanisms, and stress field properties in the Dinarides and the surrounding regions, *Geofizika*, *41*(2), 79–123, https://doi.org/10.15233/gfz.2024.41.5.

Herak, M., and D. Herak (2023), Properties of the Petrinja (Croatia) earthquake sequence of 2020–2021 – Results of seismological research for the first six months of activity, *Tectonophysics*, *858*(229885), 229,885, https://doi.org/10.1016/j.tecto.2023.229885.

Herak, M., D. Herak, and S. Markušić (1996), Revision of the earthquake catalogue and seismicity of Croatia, 1908–1992, *Terra nova*, *8*(1), 86–94, https://doi.org/10.1111/j.1365-3121.1996.tb00728.x.

Horváth, F., G. Bada, P. Szafián, G. Tari, A. Ádám, and S. Cloetingh (2006), Formation and deformation of the Pannonian Basin: constraints from observational data, *Geological Society London Memoirs*, *32*(1), 191–206, https://doi.org/10.1144/gsl.mem.2006.032.01.11.

Horváth, F., B. Musitz, A. Balázs, A. Végh, A. Uhrin, A. Nádor, B. Koroknai, N. Pap, T. Tóth, and G. Wórum (2015), Evolution of the Pannonian basin and its geothermal resources, *Geothermics*, *53*, 328–352, https://doi.org/10.1016/j.geothermics.2014.07.009.

Jamšek Rupnik, P., M. Budić, M. Vukovski, B. Kordić, M. Špelić, N. Belić, D. Palenik, N. Bočić, J. Atanackov, B. Celarc, A. Novak, M. Novak, R. Brajkovič, M. Bavec, and S. Baize (2021), Some geomorphological perspectives on the structure associated with the Petrinja M6.2 earthquake in Croatia, in *EGU General Assembly 2021*, pp. EGU21–16,578, Copernicus GmbH, Vienna, Austria, https://doi.org/10.5194/egusphere-egu21-16578.

Jamšek Rupnik, P., J. Atanackov, B. Horn, Branko Mušič, M. Zajc, C. Grützner, K. Ustaszewski, S. Tsukamoto, M. Novak, B. Milanič, A. Markelj, K. Ivančič, A. Novak, J. Jež, M. Žebre, M. Bavec, and M. Vrabec (2024), Revealing subtle active tectonic deformation: Integrating lidar, photogrammetry, field mapping, and geophysical surveys to assess the late Quaternary activity of the Sava Fault (Southern Alps, Slovenia), *Remote Sensing*, *16*(9), 1490, https://doi.org/10.3390/rs16091490.

Korbar, T. (2009), Orogenic evolution of the External Dinarides in the NE Adriatic region: a model constrained by tectonostratigraphy of Upper Cretaceous to Paleogene carbonates, *Earth-Science Reviews*, *96*(4), 296–312, https://doi.org/10.1016/j.earscirev.2009.07.004.

Li, Y., R. Bürgmann, and B. Zhao (2020), Evidence of fault immaturity from shallow slip deficit and lack of postseismic deformation of the 2017 MW 6.5 Jiuzhaigou earthquake, *Bulletin of the Seismological Society of America*, *110*(1), 154–165, https://doi.org/10.1785/0120190162.

Magyar, I., D. Radivojević, O. Sztanó, R. Synak, K. Ujszászi, and M. Pócsik (2013), Progradation of the paleo-Danube shelf margin across the Pannonian Basin during the Late Miocene and Early Pliocene, *Global and Planetary Change*, *103*, 168–173, https://doi.org/10.1016/j.gloplacha.2012.06.007.

Marchandon, M., J. Hollingsworth, and M. Radiguet (2021), Origin of the shallow slip deficit on a strike slip fault: Influence of elastic structure, topography, data coverage, and noise, *Earth and Planetary Science Letters*, *554*(116696), 116,696, https://doi.org/10.1016/j.epsl.2020.116696.

Marconato, L., P. Leloup, C. Lasserre, R. Jolivet, S. Caritg, R. Grandin, Métois, O. Cavalié, and L. Audin (2023), Insights on fault reactivation during the 2019 November 11, Mw 4.9 Le Teil earthquake in southeastern France, from a joint 3-D geological model and InSAR time-series analysis, *Geophysical Journal International*, *229*(2), 758–775.

Markušić, S. (2008), Seismicity of Croatia, in *NATO Science Series: IV: Earth and Environmental Sciences*, pp. 81–98, Springer Netherlands, Dordrecht, https://doi.org/10.1007/978-1-4020-6815-7_5.

Markušić, S., D. Stanko, D. Penava, I. Ivančić, O. Bjelotomić Oršulić, T. Korbar, and V. Sarhosis (2021), Destructive M6.2 Petrinja earthquake (Croatia) in 2020—preliminary multidisciplinary research, *Remote Sensing*, *13*(6), 1095, https://doi.org/10.3390/rs13061095.

Marone, C. J., C. H. Scholtz, and R. Bilham (1991), On the mechanics of earthquake afterslip, *Journal of Geophysical Research, [Solid Earth]*, *96*(B5), 8441–8452.

Marrero, S. M., F. M. Phillips, M. W. Caffee, and J. C. Gosse (2016), CRONUS-Earth cosmogenic 36Cl calibration, *Quaternary Geochronology*, *31*, 199–219, https://doi.org/10.1016/j.quageo.2015.10.002.

Matoš, B., M. Zajc, B. Kordić, B. Tomljenović, and A. Gosar (2017), Quaternary fault activity in the SW Pannonian Basin: GPR surveying in the Bilogora Mt.(NE Croatia), *Geological Quarterly*, *61*.

Milliner, C., R. Bürgmann, A. Inbal, T. Wang, and C. Liang (2020), Resolving the kinematics and moment release of early afterslip within the first hours following the 2016 M_w7.1 Kumamoto earthquake: Implications for the shallow slip deficit and frictional behavior of aseismic creep, *Journal of Geophysical Research. Solid Earth*, *125*(9), e2019JB018,928, https://doi.org/10.1029/2019jb018928.

Mol, J., J. Vandenberghe, and C. Kasse (2000), River response to variations of periglacial climate in mid-latitude Europe, *Geomorphology (Amsterdam, Netherlands)*, *33*(3-4), 131–148, https://doi.org/10.1016/s0169-555x(99)00126-9.

Mook, W. G., and J. van der Plicht (1999), Reporting 14C activities and concentrations, *Radiocarbon*, *41*(3), 227–239, https://doi.org/10.1017/s0033822200057106.

Moulin, A., L. Benedetti, A. Gosar, P. J. Rupnik, M. Rizza, D. Bourlès, and J.-F. Ritz (2014), Determining the present-day kinematics of the Idrija fault (Slovenia) from airborne LiDAR topography, *Tectonophysics*, *628*, 188–205, https://doi.org/10.1016/j.tecto.2014.04.043.

Moulin, A., L. Benedetti, M. Rizza, P. Jamšek Rupnik, A. Gosar, D. Bourlès, K. Keddadouche, G. Aumaître, M. Arnold, V. Guillou, and J.-F. Ritz (2016), The Dinaric fault system: Large-scale structure, rates of slip, and Plio-Pleistocene evolution of the transpressive northeastern boundary of the Adria microplate, *Tectonics*, *35*(10), 2258–2292, https://doi.org/10.1002/2016tc004188.

Mugnier, J.-L., O. Guzmán, R. Vassallo, K. Matraku, and F. Jouanne (2024), Fluvial terrace formation in a mountainous area (2): influence of eustatism, tectonics and altitudinal distribution of watersheds based on an allostratigraphic study (Albania), *Comptes rendus: Geoscience*, *356*(G1), 211–230, https://doi.org/10.5802/crgeos.278.

Métois, M., N. D'Agostino, A. Avallone, N. Chamot-Rooke, A. Rabaute, L. Duni, N. Kuka, R. Koci, and I. Georgiev (2015), Insights on continental collisional processes from GPS data: Dynamics of the peri-Adriatic belts, *Journal of Geophysical Research. Solid Earth*, *120*(12), 8701–8719, https://doi.org/10.1002/2015jb012023.

Nocquet, J.-M. (2012), Present-day kinematics of the Mediterranean: A comprehensive overview of GPS results, *Tectonophysics*, *579*, 220–242, https://doi.org/10.1016/j.tecto.2012.03.037.

Palenik, D., D. Matičec, L. Fuček, B. Matoš, M. Herak, and I. Vlahović (2019), Geological and structural setting of the Vinodol Valley (NW Adriatic, Croatia): insights into its tectonic evolution based on structural investigations, *Geologia Croatica*, *72*(3), 179–193, https://doi.org/10.4154/gc.2019.13.

Pamić, J. (2002), the sava-Vardar Zone of the Dinarides and Hellenides versus the Vardar Ocean, *Eclogae geologicae Helvetiae*.

Pavelić, D., and M. Kovačić (2018), Sedimentology and stratigraphy of the Neogene rift-type North Croatian Basin (Pannonian Basin System, Croatia): A review, *Marine and Petroleum Geology*, *91*, 455–469, https://doi.org/10.1016/j.marpetgeo.2018.01.026.

Pavičić, I., D. Rukavina, B. Matoš, and B. Tomljenović (2019), Interpretation of the tectonic evolution of the western part of the Sava Depression: structural analysis of seismic attributes and subsurface structural modeling, *Journal of Maps*, *15*(2), 733–743, https://doi.org/10.1080/17445647.2019.1663374.

Pikija, M. (1987), Osnovna geološka karta SFRJ 1: 100.000 list Sisak [Basic Geological Map of SFRY 1: 100.000, Sisak sheet–in Croatian], *Geol. Zavod Zagreb, Savezni geol. Zavod, Beograd*.

Pousse-Beltran, L., E. Nissen, E. A. Bergman, M. D. Cambaz, E. Gaudreau, E. Karasözen, and F. Tan (2020), The 2020M_w 6.8 elazığ (turkey) earthquake reveals rupture behavior of the east Anatolian fault, *Geophysical Research Letters*, *47*(13), e2020GL088,136, https://doi.org/10.102

9/2020gl088136.

Pousse-Beltran, L., L. Benedetti, J. Fleury, P. Boncio, V. Guillou, B. Pace, M. Rizza, I. Puliti, and A. Socquet (2022), 36Cl exposure dating of glacial features to constrain the slip rate along the Mt. Vettore Fault (Central Apennines, Italy), *Geomorphology (Amsterdam, Netherlands)*, *412*(108302), 108,302, https://doi.org/10.1016/j.geomorph.2022.108302.

Prelogović, E., B. Saftić, V. Kuk, J. Velić, M. Dragaš, and D. Lučić (1998), Tectonic activity in the Croatian part of the Pannonian basin, *Tectonophysics*, *297*(1-4), 283–293, https://doi.org/10.1016/s0040-1951(98)00173-5.

Ramsey, C. B. (2009), Bayesian analysis of radiocarbon dates, *Radiocarbon*, *51*(1), 337–360.

Reimer, P. J., W. E. N. Austin, E. Bard, A. Bayliss, P. G. Blackwell, C. Bronk Ramsey, M. Butzin, H. Cheng, R. L. Edwards, M. Friedrich, P. M. Grootes, T. P. Guilderson, I. Hajdas, T. J. Heaton, A. G. Hogg, K. A. Hughen, B. Kromer, S. W. Manning, R. Muscheler, J. G. Palmer, C. Pearson, J. van der Plicht, R. W. Reimer, D. A. Richards, E. M. Scott, J. R. Southon, C. S. M. Turney, L. Wacker, F. Adolphi, U. Büntgen, M. Capano, S. M. Fahrni, A. Fogtmann-Schulz, R. Friedrich, P. Köhler, S. Kudsk, F. Miyake, J. Olsen, F. Reinig, M. Sakamoto, A. Sookdeo, and S. Talamo (2020), The IntCal20 Northern hemisphere radiocarbon age calibration curve (0–55 cal kBP), *Radiocarbon*, *62*(4), 725–757, https://doi.org/10.1017/rdc.2020.41.

Rosenberg, C. L., S. Schneider, A. Scharf, A. Bertrand, K. Hammerschmidt, A. Rabaute, and J.-P. Brun (2018), Relating collisional kinematics to exhumation processes in the Eastern Alps, *Earth-Science Reviews*, *176*, 311–344, https://doi.org/10.1016/j.earscirev.2017.10.013.

Ross, Z. E., H. Kanamori, E. Hauksson, and N. Aso (2018), Dissipative intraplate faulting during the 2016 Mw 6.2 Tottori, Japan earthquake, *Journal of Geophysical Research, [Solid Earth]*, *123*(2), 1631–1642.

Royden, L. H., and F. Horváth (1988), *The Pannonian basin<subtitle>A study in basin evolution</subtitle>*, American Association of Petroleum Geologists, https://doi.org/10.1306/m45474.

Rukavina, D., B. Saftić, B. Matoš, I. Kolenković Močilac, V. Premec Fuček, and M. Cvetković (2023), Tectonostratigraphic analysis of the syn-rift infill in the Drava Basin, southwestern Pannonian Basin System, *Marine and Petroleum Geology*, *152*(106235), 106,235, https://doi.org/10.1016/j.marpetgeo.2023.106235.

Ryb, U., A. Matmon, Y. Erel, I. Haviv, A. Katz, A. Starinsky, A. Angert, and A. Team (2014), Controls on denudation rates in tectonically stable Mediterranean carbonate terrain, *Geological Society of America Bulletin*, *126*(3-4), 553–568, https://doi.org/10.1130/b30886.1.

Sadier, B., J.-J. Delannoy, L. Benedetti, D. L. Bourlès, S. Jaillet, J.-M. Geneste, A.-E. Lebatard, and M. Arnold (2012), Further constraints on the Chauvet cave artwork elaboration, *Proceedings of the National Academy of Sciences of the United States of America*, *109*(21), 8002–8006, https://doi.org/10.1073/pnas.1118593109.

Schimmelpfennig, I., L. Benedetti, R. Finkel, R. Pik, P.-H. Blard, D. Bourlès, P. Burnard, and A. Williams (2009), Sources of in-situ 36Cl in basaltic rocks. Implications for calibration of production rates, *Quaternary Geochronology*, *4*(6), 441–461, https://doi.org/10.1016/j.quageo.2009.06.003.

Schimmelpfennig, I., L. Benedetti, V. Garreta, R. Pik, P.-H. Blard, P. Burnard, D. Bourlès, R. Finkel, K. Ammon, and T. Dunai (2011), Calibration of cosmogenic 36Cl production rates from Ca and K spallation in lava flows from Mt. Etna (38°N, Italy) and Payun Matru (36°S, Argentina), *Geochimica et cosmochimica acta*, *75*(10), 2611–2632, https://doi.org/10.1016/j.gca.2011.02.013.

Schlagenhauf, A., I. Manighetti, L. Benedetti, Y. Gaudemer, R. Finkel, J. Malavieille, and K. Pou (2011), Earthquake supercycles in Central Italy, inferred from 36Cl exposure dating, *Earth and Planetary Science Letters*, *307*(3-4), 487–500, https://doi.org/10.1016/j.epsl.2011.05.022.

Schmid, S. M., D. Bernoulli, B. Fügenschuh, L. Matenco, S. Schefer, R. Schuster, M. Tischler, and K. Ustaszewski (2008), The Alpine-Carpathian-Dinaridic orogenic system: correlation and evolution of tectonic units, *Swiss Journal of Geosciences*, *101*(1), 139–183, https://doi.org/10.1007/s00015-008-1247-3.

Schmid, S. M., B. Fügenschuh, A. Kounov, L. Maţenco, P. Nievergelt, R. Oberhänsli, J. Pleuger, S. Schefer, R. Schuster, B. Tomljenović, K. Ustaszewski, and D. J. J. van Hinsbergen (2020), Tectonic units of the Alpine collision zone between Eastern Alps and western Turkey, *Gondwana Research: International Geoscience Journal*, *78*, 308–374, https://doi.org/10.1016/j.gr.2019.07.005.

Serpelloni, E., G. Vannucci, L. Anderlini, and R. A. Bennett (2016), Kinematics, seismotectonics and seismic potential of the eastern sector of the European Alps from GPS and seismic deformation data, *Tectonophysics*, *688*, 157–181, https://doi.org/10.1016/j.tecto.2016.09.026.

Siame, L., O. Bellier, R. Braucher, M. Sébrier, M. Cushing, D. Bourlès, B. Hamelin, E. Baroux, B. de Voogd, G. Raisbeck, and F. Yiou (2004), Local erosion rates versus active tectonics: cosmic ray exposure modelling in Provence (south-east France), *Earth and Planetary Science Letters*, *220*(3-4), 345–364, https://doi.org/10.1016/s0012-821x(04)00061-5.

Stone, J. O. (2000), Air pressure and cosmogenic isotope production, *Journal of Geophysical Research*, *105*(B10), 23,753–23,759, https://doi.org/10.1029/2000jb900181.

Stucchi, M., A. Rovida, A. A. Gomez Capera, P. Alexandre, T. Camelbeeck, M. B. Demircioglu, P. Gasperini, V. Kouskouna, R. M. W. Musson, M. Radulian, K. Sesetyan, S. Vilanova, D. Baumont, H. Bungum, D. Fäh, W. Lenhardt, K. Makropoulos, J. M. Martinez Solares, O. Scotti, M. Živčić, P. Albini, J. Batllo, C. Papaioannou, R. Tatevossian, M. Locati, C. Meletti, D. Viganò, and D. Giardini (2013), The SHARE European earthquake catalogue (SHEEC) 1000–1899, *Journal of Seismology*, *17*(2), 523–544, https://doi.org/10.1007/s10950-012-9335-2.

Styllas, M. N., I. Schimmelpfennig, L. Benedetti, M. Ghilardi, G. Aumaître, D. Bourlès, and K. Keddadouche (2018), Late-glacial and Holocene history of the northeast

Mediterranean mountain glaciers - New insights from in situ-produced 36Cl-based cosmic ray exposure dating of paleo-glacier deposits on Mount Olympus, Greece, *Quaternary Science Reviews*, *193*, 244–265, https://doi.org/10.1016/j.quascirev.2018.06.020.

Tari, V. (2002), Evolution of the northern and western Dinarides: a tectonostratigraphic approach, *Stephan Mueller Special Publication Series*, *1*, 223–236, https://doi.org/10.5194/smsps-1-223-2002.

Tari, V., and J. Pamić (1998), Geodynamic evolution of the northern Dinarides and the southern part of the Pannonian Basin, *Tectonophysics*, *297*(1-4), 269–281, https://doi.org/10.1016/s0040-1951(98)00172-3.

Tebbens, L. A., A. Veldkamp, W. Westerhoff, and S. B. Kroonenberg (1999), Fluvial incision and channel downcutting as a response to Late-glacial and Early Holocene climate change: the lower reach of the River Meuse (Maas), The Netherlands, *Journal of Quaternary Science: Published for the Quaternary Research Association*, *14*(1), 59–75.

Thomas, F., V. Godard, O. Bellier, L. Benedetti, V. Ollivier, M. Rizza, V. Guillou, F. Hollender, G. Aumaître, D. L. Bourlès, and K. Keddadouche (2018), Limited influence of climatic gradients on the denudation of a Mediterranean carbonate landscape, *Geomorphology (Amsterdam, Netherlands)*, *316*, 44–58, https://doi.org/10.1016/j.geomorph.2018.04.014.

Tomljenović, B., and L. Csontos (2001), Neogene–Quaternary structures in the border zone between Alps, Dinarides and Pannonian Basin (Hrvatsko zagorje and Karlovac Basins, Croatia), *International Journal of Earth Sciences*, *90*(3), 560–578, https://doi.org/10.1007/s005310000176.

Tomljenović, B., L. Csontos, E. Márton, and P. Márton (2008), Tectonic evolution of the northwestern Internal Dinarides as constrained by structures and rotation of Medvednica Mountains, North Croatia, *Geological Society Special Publication*, *298*(1), 145–167, https://doi.org/10.1144/sp298.8.

Ustaszewski, K., S. M. Schmid, B. Fügenschuh, M. Tischler, E. Kissling, and W. Spakman (2008), A map-view restoration of the Alpine-Carpathian-Dinaridic system for the Early Miocene, *Swiss Journal of Geosciences*, *101*(S1), 273–294, https://doi.org/10.1007/s00015-008-1288-7.

Ustaszewski, K., A. Kounov, S. M. Schmid, U. Schaltegger, E. Krenn, W. Frank, and B. Fügenschuh (2010), Evolution of the Adria-Europe plate boundary in the northern Dinarides: From continent-continent collision to back-arc extension: ADRIA-EUROPE PLATE BOUNDARY, DINARIDES, *Tectonics*, *29*(6), https://doi.org/10.1029/2010tc002668.

Ustaszewski, K., M. Herak, B. Tomljenović, D. Herak, and S. Matej (2014), Neotectonics of the Dinarides–Pannonian Basin transition and possible earthquake sources in the Banja Luka epicentral area, *Journal of Geodynamics*, *82*, 52–68, https://doi.org/10.1016/j.jog.2014.04.006.

van Hinsbergen, D. J. J., T. H. Torsvik, S. M. Schmid, L. C. Maţenco, M. Maffione, R. L. M. Vissers, D. Gürer, and W. Spakman (2020), Orogenic architecture of the Mediterranean region and kinematic reconstruction of its tectonic evolution since the Triassic, *Gondwana Research: International Geoscience Journal*, *81*, 79–229, https://doi.org/10.1016/j.gr.2019.07.009.

van Unen, M., L. Matenco, F. H. Nader, R. Darnault, O. Mandic, and V. Demir (2019), Kinematics of foreland-vergent crustal accretion: Inferences from the dinarides evolution, *Tectonics*, *38*(1), 49–76, https://doi.org/10.1029/2018tc005066.

Vlahović, I., J. Tišljar, I. Velić, and D. Matičec (2005), Evolution of the Adriatic Carbonate Platform: Palaeogeography, main events and depositional dynamics, *Palaeogeography, Palaeoclimatology, Palaeoecology*, *220*(3-4), 333–360, https://doi.org/10.1016/j.palaeo.2005.01.011.

Vukovski, M., M. Špelić, D. Kukoč, T. Troskot-Čorbić, T. Grgasović, D. Slovenec, and B. Tomljenović (2024), Unravelling the tectonic evolution of the Dinarides—Alps—Pannonian Basin transition zone: insights from structural analysis and low-temperature thermochronology from Ivanščica Mt., NW Croatia, *Swiss Journal of Geosciences*, *117*(1), 16, https://doi.org/10.1186/s00015-024-00464-5.

Wacha, L., B. Matoš, A. Kunz, B. Lužar-Oberiter, B. Tomljenović, and A. Banak (2018), First post-IR IRSL dating results of Quaternary deposits from Bilogora (NE Croatia): Implications for the Pleistocene relative uplift and incision rates in the area, *Quaternary International: The Journal of the International Union for Quaternary Research*, *494*, 193–210, https://doi.org/10.1016/j.quaint.2017.08.049.

Weber, J., M. Vrabec, P. Pavlovčič-Prešeren, T. Dixon, Y. Jiang, and B. Stopar (2010), GPS-derived motion of the Adriatic microplate from Istria Peninsula and Po Plain sites, and geodynamic implications, *Tectonophysics*, *483*(3-4), 214–222, https://doi.org/10.1016/j.tecto.2009.09.001.

Wei, M., D. Sandwell, and Y. Fialko (2009), A silentMw4.7 slip event of October 2006 on the Superstition Hills fault, southern California, *Journal of Geophysical Research*, *114*(B7), https://doi.org/10.1029/2008jb006135.

Xiong, W., P. Yu, W. Chen, G. Liu, B. Zhao, Z. Nie, and X. Qiao (2022), The 2020 M w 6.4 Petrinja earthquake: a dextral event with large coseismic slip highlights a complex fault system in northwestern Croatia, *Geophysical Journal International*, *228*(3), 1935–1945.

Xu, X., X. Tong, D. T. Sandwell, C. W. D. Milliner, J. F. Dolan, J. Hollingsworth, S. Leprince, and F. Ayoub (2016), Refining the shallow slip deficit, *Geophysical Journal International*, *204*(3), 1843–1862, https://doi.org/10.1093/gji/ggv563.

Zhu, S., Y. Wen, X. Gong, and J. Liu (2023), Coseismic and early postseismic deformation of the 2020 MW 6.4 Petrinja earthquake (Croatia) revealed by InSAR, *Remote Sensing*, *15*(10), 2617, https://doi.org/10.3390/rs15102617.

Zurutuza, J., A. Caporali, M. Bertocco, M. Ishchenko, O. Khoda, H. Steffen, M. Figurski, E. Parseliunas, S. Berk, and G. Nykiel (2019), The Central European GNSS Research Network (CEGRN) dataset, *Data in Brief*, *27*(104762), 104,762, https://doi.org/10.1016/j.dib.20

19.104762.

Šikić, K. (2014), Basic Geological Map of Republic Croatia 1: 100.000, Geology of the Bosanski Novi sheet, *Croatian Geological Survey*.

Špelić, M., A. Kovács, B. Saftić, and O. Sztanó (2023), Competition of deltaic feeder systems reflected by slope progradation: a high-resolution example from the Late Miocene-Pliocene, Drava Basin, Croatia, *International Journal of Earth Sciences*, *112*(3), 1023–1041, https://doi.org/10.1007/s00531-023-02290-w.

Žilić, I., M. Causse, M. Vallée, and S. Markušić (2025), High stress drop and slow rupture during the 2020 M_W6.4 intraplate Petrinja earthquake, Croatia, *Journal of Geophysical Research. Solid Earth*, *130*(1), e2024JB029,107, https://doi.org/10.1029/2024jb029107.